PHYSICAL REVIEW B **100**, 035416 (2019)

Transmission lines and resonators based on quantum Hall plasmonics: Electromagnetic field, attenuation, and coupling to qubits

S. Bosco[*] and D. P. DiVincenzo[†]
Institute for Quantum Information, RWTH Aachen University, D-52056 Aachen, Germany;
Jülich-Aachen Research Alliance (JARA), Fundamentals of Future Information Technologies, D-52425 Jülich, Germany;
and Peter Grünberg Institute, Theoretical Nanoelectronics, Forschungszentrum Jülich, D-52425 Jülich, Germany

(Received 16 January 2019; revised manuscript received 28 May 2019; published 12 July 2019)

Quantum Hall edge states have some characteristic features that can prove useful to measure and control solid state qubits. For example, their high voltage to current ratio and their dissipationless nature can be exploited to manufacture low-loss microwave transmission lines and resonators with a characteristic impedance of the order of the quantum of resistance $h/e^2 \sim 25\ \text{k}\Omega$. The high value of the impedance guarantees that the voltage per photon is high, and for this reason, high-impedance resonators can be exploited to obtain larger values of coupling to systems with a small charge dipole, e.g., spin qubits. In this paper, we provide a microscopic analysis of the physics of quantum Hall effect devices capacitively coupled to external electrodes. The electrical current in these devices is carried by edge magnetoplasmonic excitations and by using a semiclassical model, valid for a wide range of quantum Hall materials, we discuss the spatial profile of the electromagnetic field in a variety of situations of interest. Also, we perform a numerical analysis to estimate the lifetime of these excitations and, from the numerics, we extrapolate a simple fitting formula which quantifies the Q factor in quantum Hall resonators. We then explore the possibility of reaching the strong photon-qubit coupling regime, where the strength of the interaction is higher than the losses in the system. We compute the Coulomb coupling strength between the edge magnetoplasmons and singlet-triplet qubits, and we obtain values of the coupling parameter in the order of 100 MHz; comparing these values to the estimated attenuation in the resonator, we find that for realistic qubit designs the coupling can indeed be strong.

DOI: 10.1103/PhysRevB.100.035416

I. INTRODUCTION

Since its first discovery [1], the quantum Hall (QH) effect has captured the attention of researchers because of its fascinating physics and for its possible real-world applications [2,3]. A key feature which makes the QH effect so special is that over a wide range of magnetic field values and electronic densities, the bulk of the two-dimensional material is insulating, but a net electrical current can still flow. This current is carried by extended states localized at the edge of the sample, whose existence is guaranteed by a topological argument valid as long as the bulk has a mobility gap [4,5].

These edge states have several interesting properties, which make them appealing in different branches of applied science. In particular, each of these states provides a dissipationless conduction channel in dc with a quantized value of conductance e^2/h; this quantity can be measured with an extremely high precision (about a part per billion) and for this reason is now used in metrology to define the electrical resistance standard [6]. Another intriguing feature of these states is their chirality. In the context of quantum computing, the chiral and lossless nature of these edge states was invoked to propose them as a candidate for one-way processing of quantum information [7]. A different possibility is to exploit the unidirectional motion of the QH states to manufacture passive low loss nonreciprocal devices such as gyrators and circulators [8–12], that are broadly used for manipulation of qubits and noise reduction. The advantage of using the QH effect compared to other passive implementations of nonreciprocal devices [13,14] is that QH effect devices provide better scalability performances [8] and they are naturally compatible with externally applied magnetic fields, which makes them appealing for semiconductor qubits.

Materials in the QH regime have another interesting property, which was sometimes overlooked, that is they exhibit a large voltage drop between opposite edges when a low current is applied. This high voltage to current ratio is related to the large value of the quantum of resistance, $h/e^2 \sim 25\ \text{k}\Omega$; for this reason, it was pointed out that the QH effect can be exploited to manufacture low-loss transmission lines and resonators with a high characteristic impedance [15]. The characteristic impedance of these devices was estimated to be proportional to the resisitance quantum, and so orders of magnitude higher than the typical value $\sim 50\ \Omega$ of microwave circuits [16]. There has been a growing interest in high-impedance transmission lines in the quantum information community [17–21] and different implementations have been proposed [22–30]. In fact, the excitations in devices with a large characteristic impedance have a high electric field: this property can enhance the electrostatic coupling between the photon and the qubit. This enhancement is particularly attractive for semiconductor based quantum computing, where

---

[*] bosco@physik.rwth-aachen.de
[†] d.divincenzo@fz-juelich.de

the charge dipole of the qubits can be low, and it can be exploited for the challenging task of reaching the strong coupling regime, where the photon-qubit interaction strength is higher than the losses in the system [17–20,31–33].

In this paper, we focus mostly on this aspect and we analyze QH effect transmission lines and resonators. Our goal is twofold. On one hand, we provide a microscopic analysis of the electromagnetic field in these devices; on the other hand, we estimate the strength of the Coulomb interactions of the QH edge states with semiconductor spin qubits and we discuss the possibility of achieving the strong coupling regime.

We restrict our analysis to QH devices that are capacitively coupled to external electrodes [8,9]: this coupling scheme allows to manufacture low-loss devices working in the microwave domain, in contrast to Ohmic coupling, which always causes a high intrinsic contact resistance, degrading the performance [34,35]. The electrical current flowing in capacitively coupled devices is carried by low-energy and long-wavelength plasmonic excitations localized at the edge of the QH material; these excitations are usually called edge magnetoplasmons (EMPs). The physics of EMPs has been studied in depth in a variety of different cases [36–47]. We use here a semiclassical model that captures the main features of these excitations and we adapt it to describe actual devices, such as the ones in Ref. [15]. In particular, we study in detail the electromagnetic field propagating in these devices, with a particular focus on the effect of the metal electrodes and of the externally applied ac voltage sources. We also consider the effect of the Coulomb drag between EMPs propagating at different edges of a nanowire. With this analysis, we are able to justify the model of EMP propagation used in Ref. [15], and to quantify its phenomenological parameters.

Although our focus here is only on two-dimensional electron gasses in the integer QH regime, i.e., where the mobility gap in the bulk is opened by the application of a quantizing perpendicular magnetic field, with a few straightforward modifications, the results presented in this paper can be extended to a wider range of QH materials, including graphene and quantum anomalous Hall materials.

Also, to gain insight into the possibility of achieving strong photon-qubit coupling, we extend the EMP model to capture the dissipation in a QH resonator due to a finite real-valued bulk conductivity. By fitting our numerical results to a simple expression inspired by Ref. [36], we provide an analytic formula to quantify the quality (Q) factor in QH resonators: we find $Q \sim 10^3$ for commonly measured values of diagonal conductivity in the integer QH effect [48,49] and in state-of-the-art anomalous QH materials [50,51].

We then direct our attention to the electrostatic interactions between EMPs and qubits; our analysis is restricted for simplicity to singlet-triplet (ST) qubits [52]. Spin qubits do not usually work at the magnetic fields of a few tesla typically required to reach the quantum Hall regime in materials such as GaAs. However, thanks to recent technological advances, chiral edge states have been observed in more exotic materials at lower values of the magnetic field compatible with spin qubit operations. For example, experiments made on high-quality graphene-based devices show a quantized Hall conductance already at a few hundreds of millitesla [53–55], and the QH regime persist even without magnetic field in anomalous QH materials such as magnetically doped thin films of BiSe compounds [41,50,51].

We examine two possible ways of coupling the qubit to the QH resonator, namely via the coupling to the gradient of the electric field of the resonator [19] and via the coupling to the electric field of the resonator, averaged over the qubit area, which has to be mediated by an externally applied electric field [20]. We find that the effective interaction Hamiltonian is longitudinal [56–58], and that the strength of the interaction term obtained for the two mechanisms is comparable and can be in the order of 100 MHz for realistic qubit designs. Interestingly, the tunability of the second coupling mechanism via an external electric field can be used to switch on and off the photon-qubit interaction, potentially allowing for on demand control of the individual coupling terms if several qubits are coupled to the same resonator.

Using our estimation of the Q factor of the resonator, which we believe is the limiting attenuation factor in these systems, we find that the ratio between the photon-qubit interaction strength and the inverse lifetime of the EMPs can be higher than one. In particular, for realistic qubit designs, we find that this ratio can be higher than $\sim$30; this value is at least an order of magnitude larger than has been measured in recent experiments where the strong coupling regime was reached [17,18,32].

Although our analysis is restricted to a single type of qubit, we believe that our conclusions can be extended to a wider class of semiconductor spin qubits, such as single electron qubits in a magnetic field gradient and three-electron spin qubits [59].

The paper is organized as follows. In Sec. II, we discuss the semiclassical model of the EMPs. In Sec. II A, we introduce a simple approximation scheme, which allows to find a solution for the electromagnetic field that is accurate sufficiently far from the edge of QH material; we then use this solution to describe the physics of capacitively coupled QH effect devices and to justify the treatment used in Ref. [15]. In Sec. II B, we present a more detailed calculation which captures also the behavior of the electromagnetic field near the edge. In Sec. II C, we discuss the corrections to our model due to dissipation and we quantify the Q factor in QH resonators. In Sec. III, we analyze the electrostatic coupling between the resonator and a ST qubit. We compute the susceptibility of the qubit to an electric field and to its gradient and we use these results to obtain simple approximate formulas that capture the dependence of the coupling strength on the qubit design parameters. The range of validity of these formulas is examined by comparing them to a more rigorous calculation based on the explicit computation of the Hartree interaction integral. We conclude the paper by discussing in Sec. III C the possibility of reaching the strong photon-qubit coupling limit.

II. EDGE MAGNETOPLASMONS

Let us consider the two-dimensional material in the quantum Hall regime sketched in Fig. 1. In this setup, at the edge of the material, there are self-consistent charge excitations (EMPs) that are capacitively coupled to a metal electrode and that can be excited by a time-dependent voltage applied to it.

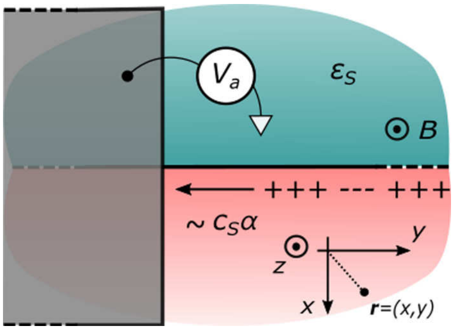

FIG. 1. Top view of the edge of a two-dimensional material (red half-plane) in the quantum Hall regime surrounded by an insulator (green region) with dielectric constant ϵ_S. The QH material supports edge excitations that are driven by an external potential V_a applied to a capacitively coupled ideal electrode (gray area). The edge magnetoplasmon propagates chirally at the boundary of the QH material with a velocity $\sim c_S\alpha$, where c_S is the speed of light in the medium and $\alpha \approx 1/137$ is the fine structure constant.

The main features of the dynamics of the EMPs are captured by a model based on the following system of partial differential equations in the frequency domain [36–38]

$$i\omega\rho(\mathbf{r},\omega) = -\nabla_{\mathbf{r}}\cdot\mathbf{j}(\mathbf{r},\omega), \tag{1a}$$

$$V(\mathbf{r},z,\omega) = V_a(\mathbf{r},z,\omega) + \int d\mathbf{r}' G(\mathbf{r},\mathbf{r}',z)\rho(\mathbf{r}',\omega), \tag{1b}$$

$$\mathbf{j}(\mathbf{r},\omega) = -\underline{\sigma}(\mathbf{r},\omega)\cdot\nabla_{\mathbf{r}}V(\mathbf{r},0,\omega). \tag{1c}$$

These equations relate the excess charge density ρ, the screened potential V [60] and the current density $\mathbf{j}$ in the (x,y) plane; here, $\mathbf{r} = (x,y)$ and $\nabla_{\mathbf{r}}$ is the two-dimensional nabla operator in the (x,y) plane. The continuity equation (1a) imposes the conservation of charge in the QH material. The screened potential V is modeled by the inverted Poisson equation (1b) with appropriate boundary conditions. It accounts for the external driving voltage applied at the metal electrodes and for the self-consistent rearrangement of charge due to Coulomb interactions. In particular, the Coulomb interactions are captured by the electrostatic Green's function G, obtained mathematically by grounding all the driving electrodes, and the effect of the external potentials is captured by the function V_a, which is the particular solution of the Laplace equation required to fix the potential of the electrodes to the appropriate time-dependent value; V_a also accounts for fringing fields. The peculiar physics of the Hall materials enters in this model through the microscopic Ohm's law (1c) via a nonreciprocal conductivity tensor

$$\underline{\sigma} = \begin{pmatrix} \sigma_{xx} & \sigma_{xy} \\ -\sigma_{xy} & \sigma_{xx} \end{pmatrix}. \tag{2}$$

Although we focus only on the integer QH effect in two-dimensional electron gasses, where the bulk conductivity is $\sigma_{xx} \approx 0$ and $\sigma_{xy} = \nu e^2/h$, by using an appropriate value of σ_{xy}, the solution presented here can be modified to describe a wide range of Hall responses, such as in graphene [42,61,62] and in anomalous QH materials [41]. In coupling to spin qubits, these materials have the advantage over GaAs of entering in the QH regime at the magnetic field values typically used for spin qubit operations [50,51,53–55].

Note that in Eq. (1c), we equated the electric field to the gradient of the scalar potential: this equality holds only in the electro-quasi-static approximation [63], where the electric field is assumed to be approximately irrotational, i.e., $\nabla_{\mathbf{r},z}\times\mathbf{E}\approx 0$ ($\nabla_{\mathbf{r},z}$ is the three-dimensional nabla operator). This approximation is justified in the low-frequency limit when the electric energy is high compared to the magnetic energy, or, analogously, when the speed of diffusion of the electric charge $v_E \sim |\mathbf{E}|/|\mathbf{B}|$ is much lower than the speed of diffusion of the electric current $\sim c_S^2/v_E$, with c_S being the speed of light in the medium, see, e.g., Sec. 3 of Ref. [64]. This condition is usually not met in conventional microwave transmission lines, where v_E and c_S are comparable, but it holds in QH droplets because $v_E \sim c_S\alpha$ [45], with α being the fine structure constant $\alpha \approx 1/137$. Additionally, since we restrict our analysis to low frequencies (compared to the bulk mobility gap), we neglect retardation effects and take the dc limit of the conductivity tensor $\underline{\sigma}(\mathbf{r},\omega\to 0) = \underline{\sigma}(\mathbf{r})$.

The model presented so far is purely classical. To analyze the physics of the edge excitations, we now evaluate the conductivity tensor in the QH limit, i.e., $\sigma_{xx} = 0$, and we find the semiclassical relation

$$i\omega\rho(\mathbf{r},\omega) = -(\nabla_{\mathbf{r},z}\sigma_{xy}(\mathbf{r}))\cdot(e_z\times\nabla_{\mathbf{r},z}V(\mathbf{r},0,\omega)). \tag{3}$$

between the charge density and the screened potential.

We use this equation to study different cases and to analyze the spatial profile of the electromagnetic fields and the attenuation of the EMPs. We begin by proposing a simple approximate solution of the equation of motion (3) based on the introduction of a phenomenological length l, which physically characterizes the width of the EMP charge density. This approximation gives a good qualitative description of the physics of the problem when $|\mathbf{r}| \gg l$ and it can be used to analyze a variety of situations. In this paper, we refer to the limits $|\mathbf{r}| \gg l$ and $|\mathbf{r}| \approx l$, respectively, as far and near field; the definition of far-field limit here differs from the conventional electromagnetic definition, where $|\mathbf{r}|$ is compared to the wavelength. A more rigorous solution of Eq. (3) capturing also near-field corrections is provided in Sec. II B. The attenuation of the EMPs caused by a finite diagonal conductivity σ_{xx} is discussed in Sec. II C.

A. Far-field analysis

1. EMPs in the half-plane

In this section, we consider a conductivity profile varying abruptly from zero to the bulk value and we model the spatial dependence of the Hall conductivity by a step function constant in the y-direction and with support in $x > 0$, i.e.,

$$\sigma_{xy}(\mathbf{r}) = \sigma_{xy}\Theta(x). \tag{4}$$

Here, $\sigma_{xy} = \nu e^2/h$ is the QH conductivity and ν is the filling factor. For now, we also neglect the effect of nearby metal electrodes and of driving potentials, and we look for self-consistent excitations at the edge of the half-plane, i.e., $V_a = 0$.

A closely related problem was solved analytically by Volkov and Mikhailov [36] by using the Wiener-Hopf decomposition. However, the solution provided there is quite complicated and, most importantly, it crucially relies on the presence of a frequency dependent complex-valued diagonal conductivity $\sigma_{xx}(\omega)$. Here, we propose instead a simpler approach that still captures the main features of the EMPs in the far-field limit.

Using the conductivity tensor in (4), Eq. (3) reduces to an integrodifferential equation for the charge density. By Fourier transforming the translational invariant y coordinate and introducing the corresponding momentum q, we obtain

$$\omega\rho(x,q,\omega) = 2\pi q\sigma_{xy}\delta(x)\int dx' G_0(x-x',q,0)\rho(x',q,\omega), \tag{5}$$

where the function

$$G_0(x,q,z) = \frac{1}{4\pi^2\epsilon_S}K_0(|q|\sqrt{x^2+z^2}), \tag{6}$$

is the Fourier transform of $G_0(\mathbf{r},\mathbf{r}',z)$ in $y-y'$ and ϵ_S is the average dielectric constant of the medium; K_0 is the modified Bessel function of the second kind. In this paper, we use the index 0 to label the electrostatic Green's function G obtained in free space, i.e., without including the effect of metal gates.

From Eq. (5), it follows that the excess charge density is proportional to $\delta(x)$; this proportionality however leads to an unphysical divergence of the integral kernel, which is related to the well-known electrostatic instability of a 1-dimensional line of charge [65]. This divergence can be dealt with by including a finite and complex-valued σ_{xx} [36]; in this case, the excess charge density spreads into the bulk with a penetration length dependent on $\mathrm{Im}(\sigma_{xx})$ and the Coulomb interactions are regularized. In this section, however, we focus on another approach to circumvent this problem, which allows for a simpler solution: we add a phenomenological length l, below which the interactions in the x direction are cut off, i.e., $\lim_{x\to 0} G_0(x,q,0) \approx G_0(l,q,0)$. With this approximation, the eigenfrequency of the EMP is

$$\omega \approx qv_0(q), \tag{7}$$

with the momentum dependent velocity

$$v_0(q) = 2\pi\sigma_{xy}G_0(l,q,0) = 2v_pK_0(|q|l), \tag{8}$$

and with a characteristic velocity

$$v_p = \frac{\sigma_{xy}}{4\pi\epsilon_S} = \frac{c\alpha}{2\pi\epsilon_S^*}\nu. \tag{9}$$

Here, c is the speed of light in vacuum, $\alpha \approx 1/137$ is the fine structure constant and ϵ_S^* is the dimensionless dielectric constant of the medium; the definition of v_p differs from the one used in Ref. [45] by a factor ν. Note the presence of a familiar $\ln(|q|)$ divergence for long wavelengths [36,38].

A more rigorous treatment of Eq. (3), not relying on the introduction of an *ad hoc* length scale to cut off the Coulomb interactions, is postponed to Sec. II B, where we consider a smoother conductivity profile, varying from zero to the bulk value in a finite length l'. Including a length l' in the calculations is another well-known procedure to avoid the divergence of G_0 and this procedure works also in the dc quantum Hall limit $\sigma_{xx}=0$ [38,39]. In atomically defined edges, l' is proportional to the magnetic length $l_B = \sqrt{\hbar/(eB)}$ and this approach is consistent also with quantum mechanical calculations [44,45,47] up to a quantum correction discussed in Appendix A. We anticipate that the EMP eigenfrequency obtained for a smoother conductivity profile, given in Eq. (58), coincides with Eq. (7) in the long-wavelength limit $l, l' \ll 1/q$ if we consider $l = c_0 l'$, with c_0 being a constant of order 1 dependent on the precise spatial profile of the conductivity. For example, for the conductivity profile in Eq. (48), we obtain $c_0 \approx 0.53$.

To find the spatial variation of the charge, potential and current density in the far-field limit, we use the approximation $\rho \propto e^{iqy}\delta(x)$ and from Eqs. (1b) and (1c), when $G = G_0$ and $V_a = 0$, we obtain

$$\rho(\mathbf{r}) \approx \rho_0\delta(x)e^{iqy}/(2\pi), \tag{10a}$$

$$V(\mathbf{r},z) \approx \rho_0 e^{iqy}G_0(x,q,z), \tag{10b}$$

$$\mathbf{j}(\mathbf{r}) \approx \rho_0\sigma_{xy}e^{iqy}\Theta(x)\begin{pmatrix}-iqG_0(x,q,0)\\ \partial_x G_0(x,q,0)\end{pmatrix}, \tag{10c}$$

with ρ_0 being a constant of units of Coulombs per meter. These results are in agreement with the asymptotic far-field limit of the solution of Volkov and Mikhailov [36] and the one presented in Sec. II B 2.

The transverse component of the current density j_x is small compared to j_y, and the potential and the current density decay into the bulk of the material on a scale $1/q$, which is generally quite long. This behavior is quite different from conventional conductors, where the skin depth is often negligible, and it is related to the fact that QH materials are a novel form of insulator, and so the electric field is unscreened in the bulk. This also implies that even if the excess charge is localized at the edge, the current density is quite broadly distributed in the material, making QH devices quite unique. Note that the electromagnetic waves traveling in this setup are not TEM modes, but more complicated hybrid TE-TM modes, with a finite component in the direction of propagation. A detailed calculation of the electric and magnetic field valid also in the near-field limit is presented in Sec. II B 2.

From a microwave engineering perspective, the complicated structure of the fields means that the choice of the reference potential is not unique, and so the definition of the characteristic impedance Z_0 of the device can vary [16]. For example, the characteristic impedance can be defined from the microwave S parameters [11,15,45] by setting it equal to the values of the impedance of the external circuit that minimizes reflection at the electrodes. Using this approach in capacitively coupled QH devices, one obtains [15]

$$Z_0 = \frac{1}{2\sigma_{xy}}. \tag{11}$$

To verify the validity of this approach, we now compare this result to the alternative definition for Z_0:

$$P = \tfrac{1}{2}Z_0I_c^2, \tag{12}$$

which relates the average power flow P to the amplitude of the conduction current I_c.

The total conduction current at position y can be found by integrating the current density in the direction of propagation over a circular cross section $\mathcal{C}$ of radius $R \to \infty$. The integration leads to

$$I_c(y) \approx \frac{v_0(q)}{2\pi}\rho_0 e^{iqy}; \tag{13}$$

to avoid the divergence of the integral at $x \to 0$, we use again the cutoff length l and we restrict the domain of integration to $[l, \infty)$. Note that at the EMP propagation frequency, the conduction current at any point in y is compensated for by a displacement current $I_d(y) \approx -\omega\rho_0 e^{iqy}/(2\pi q) = -I_c(y)$.

In the electro-quasi-static approximation, the power flow in the infinite circular cross section $\mathcal{C}$ is given by (see. e.g.. Sec. 11 of Ref. [64])

$$P = \frac{1}{2}\int_{\mathcal{C}} V(\mathbf{j}^* - i\omega\epsilon_s\mathbf{E}^*)d\mathbf{S} \approx \frac{I_c^2}{4\sigma_{xy}}, \tag{14}$$

leading to $Z_0 = 1/(2\sigma_{xy})$, in agreement with the S-parameter definition. Also, this result coincides in the long-wavelength limit with the characteristic impedance computed with the near-field solution, see Eq. (65) in Sec. II B 2.

We stress again that the definition of the characteristic impedance is not unique for non-TEM modes, see, e.g., Chapt. 3 of Ref. [16]. For example, in Ref. [43], the characteristic impedance is defined by considering the ratio of the total conduction current I_c in the direction of propagation, and the EMP potential V evaluated at position $x = l \to 0$ and $z = 0$ and measured with respect to the potential applied to an electrode nearby. In this way, the authors obtain a value of $Z_0 = 1/\sigma_{xy}$ two times larger than our estimation, see Eqs. (8), (10b), and (13). Compared to this definition, our Eq. (12) has the advantage of being independent of the arbitrary choice of reference positions where the EMP potential needs to be evaluated; of course, the response of the device is independent of the chosen definition of Z_0.

2. *Quantum Hall effect devices*

In this section, we study how the dynamics of the EMPs is affected by metal electrodes capacitively coupled to the QH material and by the driving potential applied to them. A phenomenological model of these devices [8,12,15] relies on the chiral equation of motion for the EMP charge density along the edge

$$i\omega\rho(y,\omega) = \partial_y(v(y)\rho(y,\omega)) + \sigma_{xy}\partial_y V_a(y,\omega), \tag{15}$$

and on the relation between ρ and the current in the ith electrode

$$I_i(\omega) = -i\omega\int_{\mathcal{R}_i} dy\rho(y,\omega). \tag{16}$$

The velocity $v(y)$ and the driving term $V_a(y)$ are both functions of the position along the perimeter of the droplet, parametrized by y. For simplicity, $v(y)$ and $V_a(y)$ are often approximated by piecewise functions, and so the EMPs propagate at a constant velocity in the regions $\mathcal{R}_i$ coupled to the ith electrode and are boosted by the applied voltage in a narrow region at the boundary of $\mathcal{R}_i$.

The main goal of this section is to discuss the validity of this model and to characterize the EMP velocities. To do so, we analyze the simple configuration shown in Fig. 2, which gives us valuable insight into the coupling between the edge excitations of a QH droplet and external electrodes. We consider a grounded back gate and two top gates, respectively, at a distance d_B and $d_{1,2}$ from the QH material in the z plane. The top gates 1 and 2 are placed at position $y < 0$ and $y > L_B$, respectively, and they are driven by external time-dependent potentials $V_{1,2}(\omega)$. The discussion here can then be generalized to setups with more electrodes. All the electrodes are assumed to be perfectly conducting.

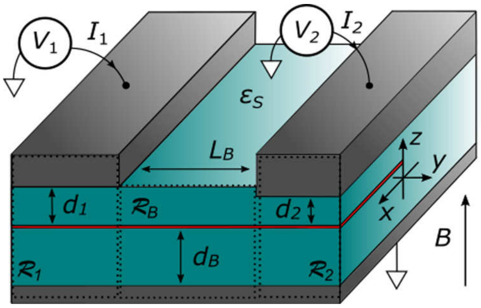

FIG. 2. Cross-section of a gated quantum Hall device. A QH material (red line) is coupled capacitively to a back gate at distance d_B and to two top gates placed at a distance $d_{1,2}$ and separated by a distance L_B in the y direction. The back gate is grounded while the ith top gate is driven by a voltage V_i, measured with respect to ground. For simplicity, all the gates extend indefinitely in the x-direction, while the QH material occupies only the half-plane $x > 0$. The y direction is divided into the three regions $\mathcal{R}_i$ characterized by the different gating configuration; $\mathcal{R}_{1,2}$ extends to $y \to \mp\infty$, respectively. The dielectric background is assumed to have a homogeneous and isotropic dielectric constant ϵ_S. An homogeneous magnetic field B is applied in the z direction.

In this configuration and in the QH regime, the EMP dynamics is captured by Eq. (3), but inverting the Poisson equation and finding the screened potential V becomes a challenging task. In fact, the two top gates break the translational invariance of the system in the y direction, so that $G(l, y-y', 0) \to G(l, y, y', 0)$, and this causes momentum mixing in the y direction. Also, in this situation, the screening potential includes a driving term V_a, which guarantees that the value of V at the boundaries matches the time-dependent applied voltage, see Eq. (1b).

To obtain an approximate equation of motion for the EMP charge which resembles Eq. (15), we divide the y direction into three different regions $\mathcal{R}_i$, with $i = (1, 2, B)$, as shown in Fig. 2. The total excess charge density ρ can then be decomposed into a sum of densities ρ_i with support only in $\mathcal{R}_i$, i.e., $\rho(x,y,\omega) = \sum_i \delta(x)\rho_i(y,\omega)$, and the equation of motion in real space reduces to

$$i\omega\rho_i(y,\omega) = \sigma_{xy}\partial_y\Bigg(V_{a,i}(0,y,0,\omega) + \sum_j\int dy' G_{ij}(l,y,y',0)\rho_j(y',\omega)\Bigg). \tag{17}$$

Here, $G_{ij}(l,y,y',0) = G(l, y\in\mathcal{R}_i, y'\in\mathcal{R}_j, 0)$ relates the charge densities of the ith and jth regions, $V_{a,i}(0,y,0,\omega) = V_a(0, y\in\mathcal{R}_i, 0, \omega)$, and we introduced again the small cut-off length l required for the integrand to be finite.

To simplify the problem, we now use a local approximation for the Green's function G, valid for smooth excitations characterized by a wavelength $1/q$ in the y direction satisfying $qd_i \ll 1$ and when $d_i/L_B \ll 1$. In this local approximation, we keep in the integral on the right-hand side of Eq. (17) only the terms that couple the charge densities in the same region, i.e., $G_{ij} \approx \delta_{ij} G_i$.

Although an exact computation of G_i is still challenging, the limiting behavior of these functions is known. In particular, far from the boundaries of $\mathcal{R}_i$, G_i can be approximately assumed to be translational invariant, and given by

$$G_i(l, q, 0) = \frac{1}{4\pi^2 \epsilon_s} \int dk \frac{e^{ikl}}{\sqrt{k^2+q^2}} f_i(\sqrt{k^2+q^2}), \qquad (18)$$

where

$$f_{1,2}(s) = (\coth(sd_{1,2}) + \coth(sd_B))^{-1}, \qquad (19a)$$

$$f_B(s) = \tfrac{1}{2}(1 - e^{-2sd_B}). \qquad (19b)$$

In the long-wavelength limit, $ql \ll 1$, these results can be used to further simplify Eq. (17) by approximating

$$G_i(l, y, y', 0) \approx 2\pi\delta(y - y')G_i(l, q \to 0, 0). \qquad (20)$$

Note that the presence of one or more metal electrodes in every region is required to regularize the $\ln(|q|)$ singularity of the EMP velocity [36] and, consequently, to guarantee that $G_i(l, q, 0)$ is finite when $ql \to 0$.

To gain insight into the driving term V_a, let us neglect the capacitive cross-talk between the two top electrodes. This approximation holds when $d_i \ll L_B$ and it allows to decouple the effects of the voltages $V_{1,2}(\omega)$ applied to the top gates; the analysis of the capacitive coupling between the electrodes can be done a posteriori, see, e.g., Refs. [10–12,15]. In this case, we obtain that well-inside $\mathcal{R}_{1,2}$ the field $V_{a,(1,2)}$ (evaluated at the position of the EMP $x = z = 0$) is approximately homogeneous and is related to $V_{1,2}(\omega)$ by

$$V_{a,(1,2)}(0, y, 0, \omega) \approx V_{1,2}(\omega)\frac{d_B}{d_B + d_{1,2}}. \qquad (21)$$

Approaching the edge of $\mathcal{R}_{1,2}$, the value of V_a in $x = z = 0$ decreases, and it vanishes in $\mathcal{R}_B$ at a distance $\sim d_{1,2}$ from the boundary. Because the driving voltage enters the equation of motion (17) via $\partial_y V_a$, the applied potential does not influence the plasmon dynamics inside $\mathcal{R}_i$, but it accelerates the EMPs at the edge of $\mathcal{R}_i$. When $d_i \ll L_B$ and in the long-wavelength limit, one can neglect the fringing effects and approximate V_a by using step functions, in agreement with the treatment presented in Ref. [45]. To illustrate this approximation, we find V_a by solving numerically the Laplace equation in the electrostatic configuration shown in Fig. 2. In Fig. 3, we show the solution V_a evaluated at $x = z = 0$ close to the boundary of $\mathcal{R}_1$ and compare it with the step function approximation obtained by neglecting fringing fields.

Let us now focus on the limit $d_{1,2} \ll d_B$, which models the response of the devices in Refs. [8,11,12,15,41]: in this case, we find that Eq. (15) holds. In particular, we obtain the piecewise equation of motion,

$$i\omega\rho_i(y, \omega) \approx v_i \partial_y \rho_i(y, \omega), \qquad (22)$$

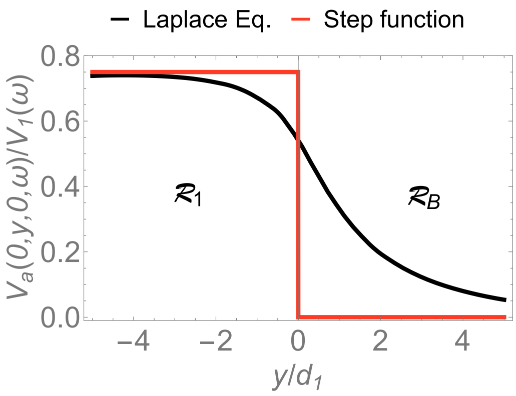

FIG. 3. Driving term $V_a(0, y, 0, \omega)$ as a function of y. We show a comparison between the numerical solution of the Laplace equation for the electrostatic configuration in Fig. 2 (black line) and the step function approximation discussed in the text (red line). The value of $V_a(0, y, 0, \omega)$ in $\mathcal{R}_1$ used for the step function is defined in Eq. (21). For the plot, we fix the ratio $d_B/d_1 = 3$ and neglect the effect of the second top electrode; the latter approximation is justified when the two electrodes are far away from each other $d_{1,2} \ll L_B$.

with velocities

$$v_i = 2\pi\sigma_{xy}G_i(l, q \to 0, 0) = v_p \ln\left(1 + \frac{4d_i^2}{l^2}\right), \qquad (23)$$

and v_p defined in Eq. (9). Also, as expected, if we neglect the fringing fields, the applied voltages $V_{1,2}$ enter in the dynamics of the EMPs only via the matching conditions at the boundaries between adjacent regions $\mathcal{R}_i$. In particular, we find that at the edge of $\mathcal{R}_{1,2}$ ρ_i satisfies

$$v_B\rho_B - v_{1,2}\rho_{1,2} = \sigma_{xy}V_{1,2}. \qquad (24)$$

Here, we used the simplified form of Eqs. (18) and (21), valid for $d_{1,2} \ll d_B$:

$$G_i(l, q, 0) \approx \frac{K_0(|q|l) - K_0\left(|q|\sqrt{l^2 + 4d_i^2}\right)}{4\pi^2\epsilon_s}, \qquad (25a)$$

$$V_{a,(1,2)}(0, y, 0, \omega) \approx V_{1,2}(\omega). \qquad (25b)$$

If we consider a side gate instead of a top gate, the EMP velocities in Eq. (23) modify as $v_i^{\mathrm{SG}} = 2v_p \ln(|2d_i/l - 1|)$; the two situations are quantitatively different only when d_i comparable to the cutoff length l.

We now analyze a more general situation, where $d_{1,2}$ and d_B are comparable. In this case, one obtains an equation of motion similar to Eq. (22), but with different EMP velocities and matching conditions. In particular, the velocities are now proportional to the long-wavelength limit of Eq. (18), and the voltages $V_{1,2}$ in the right-hand side of the matching conditions (24) acquire an additional proportionality constant $\frac{d_B}{d_B+d_{1,2}}$ dependent on the distance of the QH material from both gates, see Eq. (21).

Also, to characterize the response of a QH device, one needs to compute the current flowing in the top electrodes, which is generally given by the integral of the displacement current, i.e., by the time variation of the surface charge localized at the top gates ($\mathbf{R}_{1,2}$ indicates the two-dimensional area of the top electrodes),

$$I_{1,2}(\omega) = i\omega\epsilon_S \int_{\mathbf{R}_{1,2}} d\mathbf{r} \int d\mathbf{r}' \frac{\partial}{\partial z} G(\mathbf{r}, \mathbf{r}', d_{1,2})\rho(\mathbf{r}', \omega). \quad (26)$$

By using the same approximations discussed above, when $d_{1,2} \sim d_B$, this integral reduces to

$$I_{1,2}(\omega) \approx -i\omega \frac{d_B}{d_B + d_{1,2}} \int_{\mathcal{R}_{1,2}} dy \rho_{1,2}(y, \omega). \quad (27)$$

The prefactor $\frac{d_B}{d_B+d_{1,2}}$ in Eq. (27) is the same one that modifies the driving voltage in the matching conditions at the boundaries of $\mathcal{R}_{1,2}$. The physical origin of this term is qualitatively understood by introducing the capacitance per unit area $c_i = \epsilon_s/d_i$, which parametrizes the electrostatic coupling of the QH material to the ith metal gate. In $\mathcal{R}_{1,2}$, there are two capacitances $c_{1,2}$ and c_B in series that connect the top gate to ground: only a fraction $\frac{c_B^{-1}}{c_B^{-1}+c_{1,2}^{-1}} = \frac{d_B}{d_B+d_{1,2}}$ of the total applied voltage reaches the QH material, and, conversely, only a fraction $\frac{c_B^{-1}}{c_B^{-1}+c_{1,2}^{-1}}$ of the current flowing the QH material reaches the top gates.

In the literature, the EMP velocities are sometimes related to a capacitance per unit length $\tilde{c}$, which quantifies the Coulomb coupling of the electrode to QH edge state [8,42,43]. In the configuration examined here, the velocity in $\mathcal{R}_{1,2}$ can also be roughly estimated by considering the effect of two parallel capacitors $\tilde{c}$ by approximating Eq. (18) as

$$G_{1,2}(l, q \to 0, 0) \approx \frac{1}{2\pi} \frac{1}{\tilde{c}_B + \tilde{c}_{1,2}}, \quad (28)$$

where $\tilde{c}_i = 4\pi\epsilon_s/\ln(1 + (2d_i/l)^2)$ are obtained from the $q \to 0$ limit of Eq. (25a).

Note that the two capacitances c_i and $\tilde{c}_i$ are qualitatively different quantities: the former is the usual parallel plate capacitance (per unit area) which characterizes the electrostatic coupling between two-dimensional charged planes, while the latter characterizes the Coulomb interactions (per unit length) between a two-dimensional electrode and a (quasi-) one-dimensional line of charge.

In Ref. [15], the qualitative difference between c and $\tilde{c}$ is neglected. This is a reasonable approximation only when the edge of the QH material is very smooth and $l' \gg d_i$ (l' quantifies the broadening of $\sigma_{xy}(\mathbf{r})$ into the bulk). In fact, in this limit, one can use a fully local capacitance approximation [36,37], and assume that the Green's function in the inverted Poisson Eq. (1b) is local in both x and y and can be approximated in $\mathcal{R}_{1,2}$ as

$$G_{1,2}(\mathbf{r}, \mathbf{r}', 0) \approx \frac{\delta(\mathbf{r} - \mathbf{r}')}{\epsilon_s} \frac{d_B d_{1,2}}{d_B + d_{1,2}} = \frac{\delta(\mathbf{r} - \mathbf{r}')}{c_B + c_{1,2}}. \quad (29)$$

With this simplification, and using a linear profile of $\sigma_{xy}(\mathbf{r})$ at the edge [37], the EMP velocity in $\mathcal{R}_{1,2}$ reduces to $v_{1,2} = \sigma_{xy}/(l'(c_B + c_{1,2}))$, as used in Ref. [15]. For sharp QH edges, however, the difference between c_i and $\tilde{c}_i$ is not negligible, and one needs to adjust the results of Sec. D in Ref. [15] accordingly.

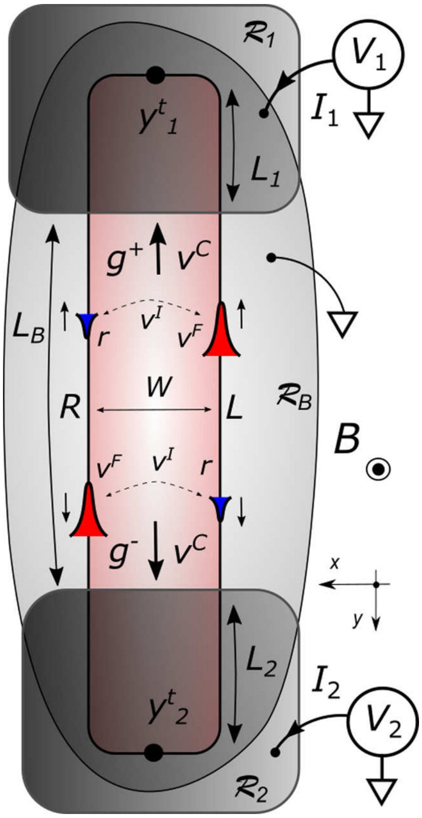

FIG. 4. Top view of a QH nanowire of width W. The nanowire is drawn in light red, while the gray areas indicate the position of the metal electrodes. The vertical cross-section of the device is shown in Fig. 2 and the y direction is divided into three regions $\mathcal{R}_i$ characterized by a different gating structure. The length of the nanowire is $y_2^t - y_1^t = L_1 + L_2 + L_B$, where y_i^t are the end points of the QH material in the y direction and L_i is the length of $\mathcal{R}_i$. The intra- and interedge Coulomb couplings are parametrized by the velocities $v^{F,I}$, respectively. The interedge component v^I causes Coulomb drag. We sketch schematically the charge profile in the x direction of the two EMP eigenmodes $g^{\pm}$, moving with velocities $\pm v^C = \pm\sqrt{(v^F)^2 - (v^I)^2}$, respectively. A positive charge (red) localized mostly at one edge drags a r times smaller negative charge (blue) at the opposite edge; in the plot the sign of $g^{\pm}$ is chosen to satisfy Eq. (46).

3. *Nanowires and Coulomb drag*

We now analyze the response of a QH nanowire of width $W \gg 2l$, such as the one shown in Fig. 4 and we focus on the effect of the Coulomb coupling between different edges. The y-direction is again divided into the three regions $\mathcal{R}_i$ shown in Fig. 2, that are characterized by a different electrostatic configuration.

According to the discussion in Sec. II A 2, the response in this setup can be modeled by studying separately the EMP dynamics in $\mathcal{R}_i$ and by appropriately matching the solutions at the boundaries to account for the applied voltage $V_{1,2}$, see Eqs. (22) and (24).

For this reason, we begin our analysis by looking for self-consistent EMP excitations in a nanowire with the conductivity profile

$$\sigma_{xy}(\mathbf{r}) = \sigma_{xy}\Theta(x)\Theta(W-x). \tag{30}$$

In this case, the equation of motion (5) in the momentum space, straightforwardly modifies as

$$\omega\rho_i(x,q,\omega) = 2\pi q\sigma_{xy}(\delta(x)-\delta(x-W)) \times \int dx' G_i(x-x',q,0)\rho_i(x',q,\omega). \tag{31}$$

Here, the index $i=(1,2,B)$ labels the electrostatic configuration of $\mathcal{R}_i$; the corresponding Green's function G_i is given by Eq. (18). It is convenient to introduce the vector decomposition of the excess charge density

$$\rho_i(x,q,\omega) = \rho_0\mathbf{g}_i(q,\omega)^T\begin{pmatrix}\delta(x)\\ -\delta(x-W)\end{pmatrix}, \tag{32}$$

which leads to the matrix eigenvalue equation

$$\omega\mathbf{g}_i(q,\omega) = q\underline{\mu}_i(q)\mathbf{g}_i(q,\omega), \tag{33}$$

with an antisymmetric velocity matrix

$$\underline{\mu}_i = \begin{pmatrix} v_i^F & -v_i^I\\ v_i^I & -v_i^F\end{pmatrix}. \tag{34}$$

The intra- and interedge velocities are defined, respectively, as

$$v_i^F = 2\pi\sigma_{xy}G_i(l,q,0), \tag{35a}$$

$$v_i^I = 2\pi\sigma_{xy}G_i(W,q,0) < v_i^F. \tag{35b}$$

Because we are interested here in understanding the effects of the interedge Coulomb coupling, we restrict our analysis to nanowires that are thin on the scale of the wavelength, i.e., $qW \ll 1$: when this condition is not met, the interedge coupling is negligible.

The antisymmetry of $\underline{\mu}_i$ is a general consequence of the Green's reciprocity theorem (i.e., $G(x,x')=G(x',x)$); also, the tracelessness of $\underline{\mu}_i$ guarantees that the eigenvalues of the matrix come in pairs with the same absolute value and opposite sign.

The matrix $\underline{\mu}_i$ is easily diagonalized: it has eigenvalues $\pm v_i^C$ with $v_i^C = \sqrt{(v_i^F)^2-(v_i^I)^2}$ and corresponding normalized eigenvectors

$$\mathbf{g}_i^\pm = \frac{1}{\sqrt{2}}\begin{pmatrix}\sqrt{1\pm\frac{v_i^C}{v_i^F}}\\ \sqrt{1\mp\frac{v_i^C}{v_i^F}}\end{pmatrix}. \tag{36}$$

The excess charge density of each eigenvector is mostly localized at one edge of the nanowire, but because of the interedge Coulomb interactions, it also drags a fraction

$$r_i = \frac{(\mathbf{g}_i^+)_R}{(\mathbf{g}_i^+)_L} = \sqrt{\frac{v_i^F-v_i^C}{v_i^F+v_i^C}} = \frac{v_i^F-v_i^C}{v_i^I} \tag{37}$$

of charge with opposite sign at the other edge. The edges of the nanowire at position $x=0$ and $x=W$ are labeled by L and R, respectively, see Fig. 4.

Let us now focus on the effect of the driving voltages. The main difference with Sec. II A 2 is that the EMP equation of motion (17) becomes here a system of coupled equations for $\mathbf{g}$. Using the local approximation for G and V_a discussed there, we obtain

$$i\omega\mathbf{g}(y,\omega) = \partial_y(\underline{\mu}(y)\mathbf{g}(y,\omega)) + \sigma_{xy}\partial_y\mathbf{V}_a(y,\omega), \tag{38}$$

where the velocity matrix $\underline{\mu}(y)$ and the driving term

$$\mathbf{V}_a(y,\omega) = \begin{pmatrix}V_a(0,y,0,\omega)\\ V_a(W,y,0,\omega)\end{pmatrix}, \tag{39}$$

are both piecewise functions with a constant value in $\mathcal{R}_i$. In particular, $\underline{\mu}(y)$ in $\mathcal{R}_i$ reduces to the $q\to 0$ limit of the matrix $\underline{\mu}_i$ in Eq. (34). Also, for the device in Fig. 4, the driving voltage is equal at the two edges, and so

$$\mathbf{V}_{a,(1,2)}(\omega) = V_{1,2}(\omega)\frac{d_B}{d_B+d_{1,2}}\begin{pmatrix}1\\1\end{pmatrix}, \tag{40}$$

and $\mathbf{V}_{a,B}=0$.

The partial differential equations (38) can be easily decoupled by introducing the matrices of column eigenvectors $M_i = (\mathbf{g}_i^+,\mathbf{g}_i^-)$, that diagonalize $\underline{\mu}_i$. Defining the EMP eigenmodes $\mathbf{u}_i \equiv M_i^{-1}\mathbf{g}_i$ and $\underline{v}_i^C = \operatorname{diag}(+v_i^C,-v_i^C)$, one obtains the equations of motion

$$i\omega\mathbf{u}_i(y,\omega) = \underline{v}_i^C\partial_y\mathbf{u}_i(y,\omega), \tag{41}$$

and the matching conditions

$$\underline{v}_B^C\mathbf{u}_B - \underline{v}_{1,2}^C\mathbf{u}_{1,2} = \sigma_{xy}M_{1,2}^{-1}\mathbf{V}_{a,(1,2)}(\omega). \tag{42}$$

Note that using Eq. (40), the right-hand side of (42) simplifies to $\sigma_{xy}\Gamma_{1,2}V_{1,2}\frac{d_B}{d_B+d_{1,2}}(1,1)^T$, with

$$\Gamma_{1,2} = \frac{v_{1,2}^F}{\sqrt{2}v_{1,2}^C}\left(\sqrt{1+\frac{v_{1,2}^C}{v_{1,2}^F}}-\sqrt{1-\frac{v_{1,2}^C}{v_{1,2}^F}}\right). \tag{43}$$

We can now find the total current $I_{1,2}$ flowing into the top gates in $\mathcal{R}_{1,2}$, which is obtained by integrating the excess charge density $\rho_{1,2}$. In a nanowire, $I_{1,2}$ is composed of the sum of the contributions of the two counter-propagating EMP eigenmodes $u_{1,2}^\pm$ (± indicates the sign of the velocity), i.e.,

$$I_{1,2} = \frac{1}{\sqrt{2}}\left(\sqrt{1+\frac{v_{1,2}^C}{v_{1,2}^F}}I_{1,2}^+ + \sqrt{1-\frac{v_{1,2}^C}{v_{1,2}^F}}I_{1,2}^-\right), \tag{44}$$

with

$$I_{1,2}^\pm = -i\omega\frac{d_B}{d_B+d_{1,2}}\int_{\mathcal{R}_{1,2}} dy\, u_{1,2}^\pm(y,\omega). \tag{45}$$

Note that the setup in Fig. 4 is a closed device, and so to proceed further in our analysis, we need to model the termination of the nanowire. For simplicity, we assume, that the nanowire is thin, i.e., $W\ll L_i$; in this limit, one can neglect the dynamics of the EMP in the x direction, and require that at the end points y_i^t of the wire, the normal component of the current density vanishes. In terms of the EMP eigenmodes $u_{1,2}^\pm$, this boundary condition reduces to

$$u_{1,2}^+(y=y_{1,2}^t) = -u_{1,2}^-(y=y_{1,2}^t). \tag{46}$$

Using this condition and Eq. (44), we find that $I^{+}_{1,2} = I^{-}_{1,2}$ for the device in Fig. 4, and so, the total current flowing in the top gates reduces to $I_{1,2} = I^{+}_{1,2}/\Gamma_{1,2}$. Note now that because of the prefactor of the inhomogeneous term in Eq. (42), one obtains that $I^{+}_{1,2} \propto \Gamma_{1,2}$, and so the total current $I_{1,2}$ is independent of $\Gamma_{1,2}$.

Consequently, we find that the port voltages $(V_1, V_2)^T$ and the currents $(I_1, I_2)^T$ are related by the 2×2 port-impedance matrix

$$\frac{-i}{2\sigma_{xy}}\begin{pmatrix}\cot\left(\frac{\Omega_1^C}{2}\right)+\cot\left(\Omega_B^C\right) & \csc\left(\Omega_B^C\right)\\ \csc\left(\Omega_B^C\right) & \cot\left(\frac{\Omega_2^C}{2}\right)+\cot\left(\Omega_B^C\right)\end{pmatrix}, \tag{47}$$

where we defined the dimensionless parameter $\Omega_i^C = \omega L_i/v_i^C$. This result is consistent with the terminal-wise admittance matrix reported in Eq. (4) of [15], that was obtained excluding the interedge interactions; in our case, the EMP velocities v_i^C are renormalized by the Coulomb drag.

Also, Eqs. (44) and (46) justify the equivalent circuit model for these devices proposed in Ref. [15], where there are two circuits characterized by two charge densities with opposite sign and moving in opposite direction connected in parallel. These charge densities are sketched in Fig. 4 as the blue and red components of $g^{\pm}$; in the plot their sign is chosen to satisfy Eq. (46).

B. Near-field analysis

In this section, we provide a more detailed discussion of the electromagnetic field at the edge of a QH droplet, which accounts also for near-field corrections. For simplicity, we now neglect the driving voltage and study only self-consistent plasmonic excitations in a half-plane.

As discussed in Sec. II A, in the QH limit ($\sigma_{xx} \to 0$) and for sharp edges, a purely classical model of the EMPs has a pathology due to the electrostatic instability of a one-dimensional line of charge [65]. This issue can be resolved by considering a conductivity tensor with a small but finite broadening l' into the bulk of the material. For example, we consider a conductivity profile of the form

$$\sigma_{xy}(\mathbf{r}) = \frac{\sigma_{xy}}{2}\left(1+\operatorname{erf}\left(\frac{x}{l'}\right)\right). \tag{48}$$

Because of the spatial dependence of the conductivity, the delta function in Eq. (5) becomes a normalized gaussian and so the excess charge density takes now the form $\rho(\mathbf{r}) \propto \partial_x\sigma_{xy}(\mathbf{r}) \propto e^{-(x/l')^2}$.

Note that the length l' is a phenomenological parameter, whose value has to be extracted from experiments or computed a priori. Here, to estimate l', we fit the excess charge density ρ and the eigenfrequency ω obtained in our semiclassical model against the results obtained from a quantum mechanical analysis [44–46]. A more detailed explanation of the quantum mechanical treatment, including a discussion of the leading quantum corrections to the EMP dynamics, can be found in Appendix A. In particular, we find that in QH droplets with atomically defined edges and filling factors $\nu = 1$, the EMP charge density is also approximately gaussian, see Fig. 14 a), and so the conductivity (48) is well-suited to model these systems.

In this case, a good agreement of the results is achieved when $l' \propto l_B$, with $l_B = \sqrt{\hbar/(eB)}$ being the magnetic length; the proportionality constant is of order one and its value depends on the Fermi energy of the QH material. For example, when the Fermi energy lies in the middle of the cyclotron gap between the lowest and first Landau level,

$$l' \approx 0.75 l_B. \tag{49}$$

Also, from the quantum mechanical treatment presented in Appendix A, it follows that the conductivity profile in Eq. (48) is not centered at the physical edge of the QH material, but is shifted into the bulk by a length $x_0 \propto l_B$. In particular, at the same Fermi energy that gives (49), we obtain

$$x_0 \approx 1.15 l_B. \tag{50}$$

The precise value of l' and x_0 is relevant for the discussion of the resonator-qubit coupling in Sec. III. The general dependence of l' and x_0 on the Fermi energy is shown in Fig. 14(b).

1. EMP velocity

When no external voltage is applied, Eq. (3) with the conductivity profile (48) reduces to a homogeneous Fredholm integral equation of the second kind, that has to be solved for the EMP charge density ρ and for the eigenfrequency ω. There are several possible ways to proceed: we choose here an approach that can be easily generalized to include a finite diagonal conductivity, as described in Sec. II C.

We work in the momentum space ($y \to q$), and we introduce the auxiliary function p defined by

$$\rho(x,q,\omega) = p(x,q,\omega)\frac{e^{-(x/l')^2}}{\sqrt{\pi}l'}. \tag{51}$$

For simplicity of notation, we suppress the explicit dependence of p on q and ω. Also, we neglect at first the effect of the electrodes, and so we use the free space Green's function (6). The EMP equation of motion reduces to

$$\frac{\omega}{qv_p}p(x) = \frac{2}{\sqrt{\pi}l'}\int_{\mathbb{R}} dx' e^{-(x'/l')^2}K_0(|q||x-x'|)p(x'). \tag{52}$$

This integral equation can be converted into a matrix eigenvalue problem by using the decomposition

$$p(x) = \sum_{n=0}^{\infty} p_n\sqrt{n+\frac{1}{2}}P_n\left(\operatorname{erf}\left(\frac{x}{l'}\right)\right), \tag{53}$$

where P_n are the Legendre polynomials [66]. This leads to

$$\frac{\omega}{qv_p}p_n = \sum_{m=0}^{\infty}\Lambda_{nm}p_m, \tag{54}$$

with

$$\Lambda_{nm} = \sqrt{n+\frac{1}{2}}\sqrt{m+\frac{1}{2}}\int_{-1}^{1} ds P_n(s)\int_{-1}^{1} ds' P_m(s') \times K_0(|ql'||\operatorname{erf}^{-1}(s)-\operatorname{erf}^{-1}(s')|), \tag{55}$$

and with erf^{-1} being the inverse error function.

Note that although the matrix problem in Eq. (54) supports an infinite number of eigenvalues, in the sharp edge limit, the slower (acoustic) modes are strongly damped and weakly

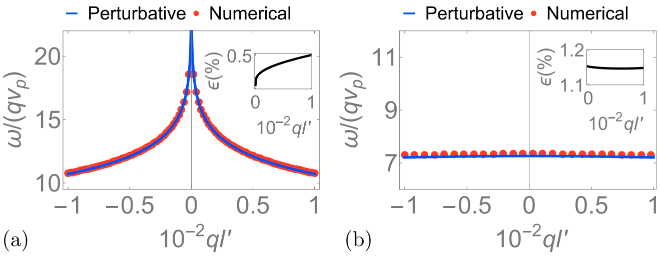

FIG. 5. Eigenvalues of Eq. (54): comparison between the numerical results and the perturbative solution (58). In the insets, we plot the percentage error in making the approximation. In (a), we plot the eigenfrequency without considering screening gates, while in (b), we include a top gate at distance $d = 10l'$ from the EMP.

coupled to external voltage sources [38,45]; for this reason, we neglect them here and focus only on the fastest (optical) mode. Taking the long-wavelength limit $ql' \to 0$ in the kernel of the integral (55), we obtain

$$\Lambda_{nm} \approx -\ln\left(\frac{(ql')^2 e^{\gamma}}{8}\right)\delta_{n0}\delta_{m0} - \tilde{\Lambda}_{nm}, \qquad (56)$$

with γ being the Euler constant and with

$$\tilde{\Lambda}_{nm} = \ln(2e^{\gamma})\delta_{n0}\delta_{m0} + \sqrt{n+\frac{1}{2}}\sqrt{m+\frac{1}{2}}\int_{-1}^{1} ds P_n(s) \times \int_{-1}^{1} ds' P_m(s') \ln(|\mathrm{erf}^{-1}(s) - \mathrm{erf}^{-1}(s')|). \qquad (57)$$

The first term in Eq. (57) guarantees that $\tilde{\Lambda}_{00} = 0$. This decomposition is useful for perturbative considerations: for long wavelengths, the dominant term in the eigenvalue equation (54) is the divergent term at $n = m = 0$. This implies that the EMP eigenfrequency in this limit can be approximated as

$$\omega \approx -qv_p \ln\left(\frac{(ql')^2 e^{\gamma}}{8}\right), \qquad (58)$$

and the EMP charge density (51) preserves the gaussian form, i.e., $p_n \approx \delta_{n0}$ in Eq. (53). This solution is consistent with the quantum analysis in Appendix A and it also qualitatively agrees with the results of the smooth edge model of Aleiner and Glazman [38,39].

It is also straightforward to modify the interaction kernel in the definition of Λ_{nm} (55) to include the effects of external electrodes. For example, we consider now a top gate at a distance d from the EMP. As discussed in Sec. II A 2, the metal electrode regularizes the long-wavelength behavior of the EMP because of the positive image charge at $z = 2d$, see Eq. (25a). For this reason, when the gate is very close to the EMP, the perturbative treatment just presented becomes questionable; we find however that it still gives an excellent approximation, with an error below 4% for $d \gtrsim 2l'$ at $q = 0$.

A comparison between numerics and the perturbative expansion for small wave vectors with and without electrodes is shown in Fig. 5: the correction due to $\tilde{\Lambda}$ is negligible in the parameter regime we are interested in.

At this point, we can also compare this result to the simple solution proposed in Sec. II A: we find that in the longwavelength limit the eigenfrequencies in Eqs. (7) and (58) coincide when

$$l = c_0 l', \quad \text{with } c_0 = \frac{e^{-\gamma/2}}{\sqrt{2}} \approx 0.53; \qquad (59)$$

the same value of l is appropriate in the presence of electrodes.

For different conductivity profiles, one can proceed in a similar way. In the long-wavelength limit, we find that the excess charge density takes again the form $\rho(\mathbf{r}) \propto \partial_x \sigma_{xy}(\mathbf{r})$ and the eigenfrequency can be estimated from the far-field Eqs. (7) and (8), but with a different value of c_0, which depends on the conductivity profile chosen. For example, using $\sigma_{xy}(\mathbf{r}) \propto \arctan(\sqrt{x/l'})$, we obtain $c_0 = 4$, in agreement with the solution of Ref. [38].

2. Electromagnetic field

Here, we discuss the near-field behavior of the electromagnetic field and compare it to the results presented in Sec. II A. To do so, we use the perturbative solution to the eigenvalue problem (54): we neglect the corrections caused by $\tilde{\Lambda}_{nm}$ and consider a gaussian charge density with broadening l'. Without electrodes, the charge, potential and current are given by

$$\rho(\mathbf{r}) = \rho_0 e^{iqy} e^{-\left(\frac{x}{l'}\right)^2}/(2\pi\sqrt{\pi}l'), \qquad (60a)$$

$$V(\mathbf{r}, z) = V_0 e^{iqy} \mathcal{G}_0(x, q, z), \qquad (60b)$$

$$\mathbf{j}(\mathbf{r}) = V_0 e^{iqy} \sigma_{xy}(\mathbf{r}) \begin{pmatrix} -iqg_0(x, q) \\ \partial_x g_0(x, q) \end{pmatrix}, \qquad (60c)$$

and they have to be compared to their far-field counterparts in Eq. (10).

Here, ρ_0 is a unspecified constant of units charge per meter, we defined $V_0 = \rho_0/(8\pi^2\epsilon_S)$ and $\sigma_{xy}(\mathbf{r})$ is given in Eq. (48). The dimensionless function $\mathcal{G}$ depends on the specific electrostatic configuration and in free space is

$$\mathcal{G}_0(x, q, z) = \frac{2}{\sqrt{\pi}l'}\int_{\mathbb{R}} dx' e^{-\left(\frac{x-x'}{l'}\right)^2} K_0(|q|\sqrt{x'^2 + z^2}). \qquad (61)$$

The value of $\mathcal{G}_0$ on the $z = 0$ plane is particularly important for the qubit coupling described in Sec. III B, and so we define $\mathcal{G}_0(x, q, 0) \equiv g_0(x, q)$. We now analyze two useful asymptotic limits of g_0, namely $|q|^{-1} \gg x, l'$ and $l' \ll |q|^{-1}, x$. The first limit is useful to have a good estimation of g_0 in the near field, i.e., when x and l' are of the same order of magnitude and both much smaller than $1/q$, while the second limit gives a better estimation in the far field, and, more generally, when the argument of the Bessel function is not infinitesimal. In the former case, we expand the Bessel function to the lowest order in $|q|$ and perform the integration, leading to

$$g_0(x, q) \approx {}_1F_1^{(1,0,0)}\left(0; \frac{1}{2}; -\frac{x^2}{l'^2}\right) - \ln\left(\frac{(ql')^2 e^{\gamma}}{16}\right), \qquad (62)$$

with ${}_1F_1^{(1,0,0)}$ being the derivative with respect to the first argument of the Kummer function of the first kind [66]. In contrast, in the far-field limit, we approximate the gaussian by a delta function as in Sec. II A, and we obtain

$$g_0(x, q) \approx 2K_0(|qx|). \qquad (63)$$

The two different approximations are shown in Fig. 6.

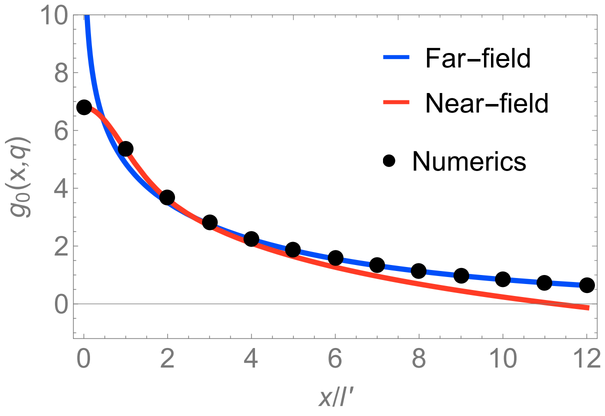

FIG. 6. Near- and far-field approximations of the function $g_0(x, q)$, defined by the limit $z \to 0$ of Eq. (61). The black dots are obtained by solving the integral numerically, while the solid red and blue lines are the asymptotic solution in the near- and far-field limits, respectively. For illustrative purposes, we used a rather high value of $ql' = 0.1$.

From Eq. (60), it is straightforward to compute the electric and magnetic fields

$$\mathbf{E}(\mathbf{r}) \approx -\nabla_{\mathbf{r},z} V(\mathbf{r}, z), \tag{64a}$$

$$\mathbf{B}(\mathbf{r}) = \frac{1}{c_S^2} \nabla_{\mathbf{r},z} \times \int d\mathbf{r}' G_0(\mathbf{r}, \mathbf{r}', z) \begin{pmatrix} \mathbf{j}(\mathbf{r}') \\ 0 \end{pmatrix}, \tag{64b}$$

where once again we use the electro-quasi-static approximation for **E** and neglected the small corrections due to the time derivative of **B** (i.e., $\nabla \times \mathbf{E} \approx 0$). In Eq. (64b), we use $\mathbf{B} = \nabla \times \mathbf{A}$, where **A** is the vector potential in the Lorenz gauge [67]. Figure 7 shows a comparison of the electromagnetic fields in the cross section $y = 0$ obtained from Eq. (60) and from its far-field limit (10). In the plots, we consider two QH materials lying in the (x, y) plane with a smooth and an abrupt conductivity profile and we neglect the effect of the external electrodes.

We can also verify the estimation of the impedance given in Sec. II A. The conduction current I_c can be computed without resorting to an artificial cutoff length, and we find that Eq. (13) is still applicable. Also, to find the power flow, we start from the usual definition of the Poynting vector $\mathbf{S} = \frac{1}{2}\mathbf{E} \times \mathbf{H}^*$ and we resort to the electro-quasi-static approximation $\nabla \times \mathbf{E} \approx 0$, such that, up to a unimportant curl, $\mathbf{S} \approx \frac{1}{2} V(\mathbf{j} + i\omega\epsilon_S \mathbf{E})^*$, see, e.g., Sec. 11 of Ref. [64]. Integrating **S** along a circular cross-section with radius $R \to \infty$ in the $y = 0$ plane, the average power flow reduces to

$$P = \frac{I_c^2}{4\sigma_{xy}}(1 - h(q)). \tag{65}$$

The function $h(q) \propto e^{-(ql'/2)^2}/K_0((ql'/2)^2)$ can be discarded in the long-wavelength limit, and so we obtain the same result as Eq. (14).

To conclude this section, we comment on the effect of a top and of a side gate at distance d from the edge of the QH material. The function $\mathcal{G}_0$ in (61) is modified as $\mathcal{G}_0 \to \mathcal{G}_0 + \mathcal{G}_{t,s}$, where the additive corrections are

$$\mathcal{G}_t = -\int_{\mathbb{R}} \frac{2d'}{\sqrt{\pi} l'} e^{-(\frac{x-x'}{l'})^2} K_0(|q|\sqrt{x'^2 + (z + 2d)^2}), \tag{66a}$$

$$\mathcal{G}_s = -\int_{-d}^{\infty} \frac{2dx'}{\sqrt{\pi} l'} e^{-(\frac{x-x'}{l'})^2} K_0(|q|\sqrt{(x + x' + 2d)^2 + z^2}), \tag{66b}$$

for the top and side gate, respectively.

We are interested in understanding the effect of the electrodes on the electric field and on its gradient in the $z = 0$

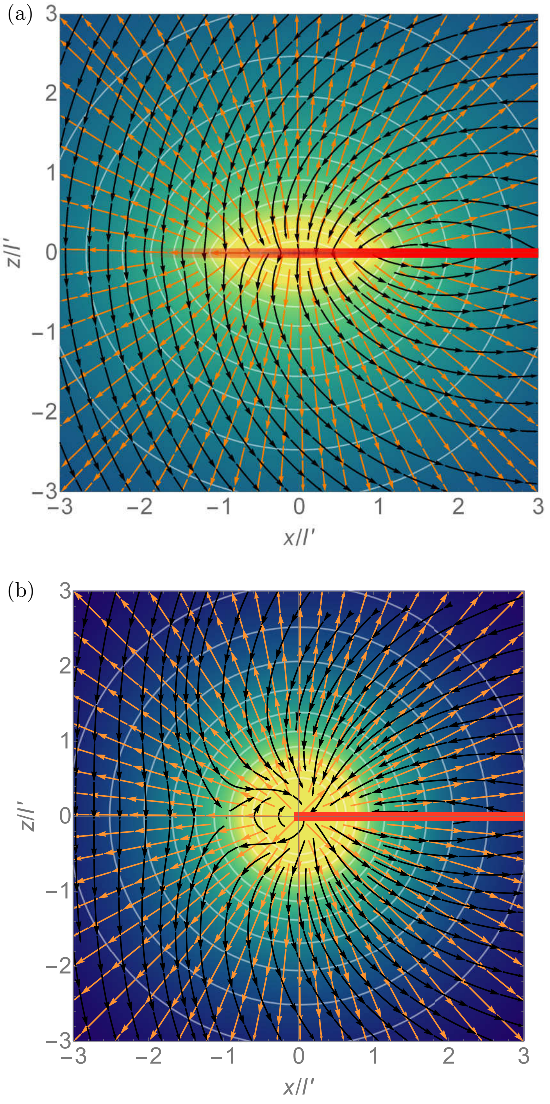

FIG. 7. Electromagnetic field in the plane $y = 0$ generated by a QH material in the (x, y) plane and without electrodes. In (a), we show the results obtained by the potential and current density in Eq. (60), and in (b), we show the analogous far field obtained from Eq. (10). In the plots, we choose $ql' = 0.01$ and the axis are in units $l' = l/c_0$ with $c_0 = 0.53$. The orange (black) stream lines represent the electric (magnetic) field, while in the background, we plotted the scalar potential V. The thick red lines indicate the position of the QH material, and their opacity is weighted by the conductivity profile.

plane, where, in Sec. III, we place the qubit. To do so, the far-field asymptotic limit of the integrals $g_{t,s} \equiv \mathcal{G}_{t,s}(z \to 0)$ suffices, because for a finite value of d the argument of the Bessel function does not diverge. By approximating the gaussian in the integrand (66) by a delta function, it is straightforward to verify that the electric field in x direction decreases (increases) by introducing a top (side) gate. In contrast, the electric field gradient always decreases when we consider a side gate, while for a top gate the behavior depends on d: the gradient increases if $d > x/2$ and it decreases otherwise.

C. Dissipation

In this section, we extend the semiclassical model presented of Sec. II B 1 to include dissipation and we present a simple fitting of the results inspired by the analytic solution of [36].

The decay of the EMPs is assumed to be caused by a finite and real diagonal part $\sigma_{xx}(\mathbf{r})$ of the conductivity tensor in the system of equations (1). Imperfections in the dielectric or in the electrodes are neglected and can be accounted for *a posteriori* [16]. Because of σ_{xx}, the relation in Eq. (3) between the charge density and the screened potential is modified by the additional term in the right-hand side

$$\sigma_{xx}(\mathbf{r})\nabla^2_{\mathbf{r}}V(\mathbf{r},0,\omega) + (\nabla_{\mathbf{r}}\sigma_{xx}(\mathbf{r}))\cdot\nabla_{\mathbf{r}}V(\mathbf{r},0,\omega). \tag{67}$$

For simplicity, we now restrict our analysis to self-consistent excitations in a half-plane. We use the form of (48) for the two components of the conductivity tensor $\sigma_{xx}(\mathbf{r})$ and $\sigma_{xy}(\mathbf{r})$. We also neglect retardation effects and take the dc limit of the conductivity.

Fourier transforming the y direction and using the free space Green's function (6), we obtain an integral equation for the auxiliary function $p(x)$ similar to Eq. (52) with the additional integral in the right-hand side

$$-i\frac{2\sigma_{xx}}{\sqrt{\pi}\sigma_{xy}ql'}\hat{D}(x)\int_{\mathbb{R}}dx' e^{-(x'/l')^2}K_0(|q||x-x'|)p(x'), \tag{68}$$

where we define the differential operator

$$\hat{D}(x) = \partial_x + \frac{\sigma_{xx}(\mathbf{r})}{\partial_x\sigma_{xx}(\mathbf{r})}\left(\partial^2_{xx} - q^2\right). \tag{69}$$

Following the procedure presented in Sec. II B 1, we discretize the integral equation by using the decomposition (53) and we obtain the eigenvalue equation (54) with the extra imaginary term

$$-i\frac{\sigma_{xx}}{\sigma_{xy}ql'}\sum_{m=0}^{\infty}\sum_{k=0}^{\infty}\mathcal{D}_{nk}\Lambda_{km}p_m, \tag{70}$$

with

$$\mathcal{D}_{nk} = \frac{2}{\sqrt{\pi}}\sqrt{n+\frac{1}{2}}\sqrt{k+\frac{1}{2}}\int_{\mathbb{R}}dx e^{-x^2/l'^2} \times P_n\left(\operatorname{erf}\left(\frac{x}{l'}\right)\right)\hat{D}(x)P_k\left(\operatorname{erf}\left(\frac{x}{l'}\right)\right). \tag{71}$$

Therefore the problem including dissipation reduces to the diagonalization of the complex-valued matrix

$$\Lambda_D = \left(\mathcal{I} - i\frac{\sigma_{xx}}{\sigma_{xy}ql'}\mathcal{D}\right)\Lambda, \tag{72}$$

with $\mathcal{I}$ being the identity matrix.

For long wavelengths, we approximate Λ by Eq. (56) and neglect the q^2 correction in Eq. (69). To find the complex EMP eigenfrequency ω, we diagonalize Λ_D numerically.

In Fig. 8(a), we show how $\operatorname{Im}(\omega)$ varies as a function of the wave vector q for different values of σ_{xx}/σ_{xy}. Note that the dissipative term $\operatorname{Im}(\Lambda_D)$ is proportional to the ratio of two small parameters $\sigma_{xx}/(\sigma_{xy}ql')$, and so it is not necessarily small. Therefore, even for small values of the diagonal conductivity, one cannot generally neglect the redistribution of charges in the bulk due to σ_{xx} [36]. However, the matrix element $(\mathcal{D}\Lambda)_{00} = 0$ and so in the long-wavelength and small dissipation limit (and when $\sigma_{xx}/(\sigma_{xy}ql') \lesssim 1$), Eq. (58) still gives a good estimation of $\operatorname{Re}(\omega)$. The dependence of $\operatorname{Im}(\omega)$ on the ratio of diagonal to off-diagonal conductivities σ_{xx}/σ_{xy} obtained for $ql' = 10^{-3}$ is shown in Fig. 8(c).

Our numerical solution can be interpreted by considering the analytical solution of a closely related problem, provided by Volkov and Mikhailov [36]. They consider a very sharp edge, modeled by $\underline{\sigma}(\mathbf{r}) \propto \Theta(x)$, and a frequency dependent diagonal conductivity of the form $\sigma_{xx}(1 + i\omega T)$, with T being a characteristic scattering time. The imaginary part of σ_{xx} is related to the kinetic inductance of the QH material.

In free space and for long wavelengths, they calculated a EMP propagation velocity $\omega/q \approx -2v_p \ln(|q|l)$, where, most importantly, l is a complex number with the units of length: the lifetime of the EMP is then parametrized by the imaginary part of l. In particular, they find

$$l \propto -i\frac{v_p}{\omega}\frac{\sigma_{xx}}{\sigma_{xy}}(1 + i\omega T). \tag{73}$$

We remark that the presence of an imaginary part of σ_{xx} in their treatment is required to avoid singularities of the Coulomb interaction kernel. In contrast, if one considers the smoother profile of the conductivity (48), varying from zero to the bulk value over a finite length l', the problem is well-defined even for $\operatorname{Im}(\sigma_{xx}) = 0$, as discussed in Sec. II B. In this case, we find that $\operatorname{Im}(\omega)$ can be well approximated by using the far-field eigenfrequency ω in Eqs. (7) and (8), with the complex-valued length

$$l \approx c_0\left(l' - i\pi\frac{v_p}{\omega_0}\frac{\sigma_{xx}}{\sigma_{xy}}\right) \equiv l_0 - il_1, \tag{74}$$

where $\omega_0 \equiv \omega(\sigma_{xx} \to 0) \in \mathbb{R}$, and c_0 is the dimensionless constant defined in Eq. (59).

From Figs. 8(a) and 8(c), we observe that this estimation works reasonably well when $l_0 \gtrsim l_1$, i.e., $\sigma_{xx}/\sigma_{xy} \lesssim ql'$, and that it overestimates dissipation otherwise. In particular, when $\sigma_{xx}/\sigma_{xy} = 10^{-4}$, the agreement is excellent in the range of wavelengths considered. For higher values of σ_{xx}/σ_{xy}, the approximation becomes worse at short wave vectors ql'. In fact, for small values of ql', the numerical analysis suggests a finite value of attenuation, while the approximation scales as $\sim 1/q$ because of the divergence of $l_1 = \operatorname{Im}(l)$ in Eq. (74), and so the approximation overestimates the attenuation of the

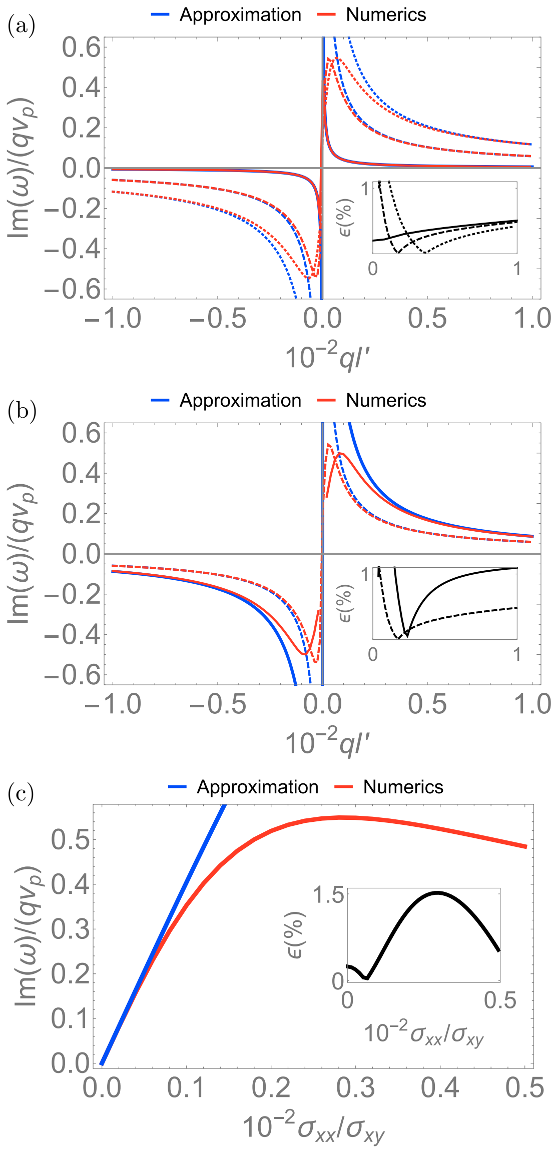

FIG. 8. Attenuation of the EMPs: $\mathrm{Im}(\omega)$. The red lines are computed numerically by diagonalizing (72), while the blue lines are obtained by using the complex-valued length l (74) in the far-field EMP eigenfrequency (7), with the appropriate velocity dependent on the electrostatic configuration. In the insets, we plot the percentage error made in $\mathrm{Re}(\omega)$ by this approximation. In (a) and (b), we plot $\mathrm{Im}(\omega)$ as a function of the wave vector ql' at a fixed value of the diagonal conductivity. In (a), we do not include metal gates and use (6). The solid, dashed and dotted lines are obtained for $\sigma_{xx}/\sigma_{xy} = 10^{-4}$, $\sigma_{xx}/\sigma_{xy} = 10^{-3}$, and $\sigma_{xx}/\sigma_{xy} = 2\times 10^{-3}$, respectively. In (b), we show the effect of a top gate and use (25a). We consider $\sigma_{xx}/\sigma_{xy} = 10^{-3}$ and plot with a solid line the value of $\mathrm{Im}(\omega)$ including a top gate at distance $d = 10l'$; the dashed line is shown for comparison and is obtained without gates. In (c), we plot $\mathrm{Im}(\omega)$ as a function of the ratio of diagonal to off-diagonal conductivity σ_{xx}/σ_{xy} and we use $ql' = 10^{-3}$.

EMPs. Also, in the range of parameters considered, the real part of the propagation frequency $\mathrm{Re}(\omega)$ does not change appreciably.

Let us compare our result with the experiment in Ref. [68]. Here, the authors characterize the propagation of a EMP wavepacket in a large etched mesa with a diameter of 0.54 mm. From their data at $B = 5.1$ T, corresponding to $\nu = 1$, one can extract an average velocity of the wave packet of 4×10^5 m/s. Comparing this value with the our Eq. (8), we find $|q|l \approx 0.0076$. Here, we identify q with the average momentum of the wave packet and not with the momentum of the fundamental mode $q = 2\pi/L_y$, as in the reference.

To obtain the decay rate, one needs to know the ratio σ_{xx}/σ_{xy}. We consider the realistic ratio $\sigma_{xx}/\sigma_{xy} = 10^{-3}$, that corresponds to the resistance per square $\rho_{xx} \approx 50\ \Omega$, in agreement with the value measured in a similar sample in Ref. [12]. Using this value, and combining Eqs. (58) and (74) (and with $c_0 = 0.53$ and $l'/l_B = 0.75$), we obtain the decay rate $\mathrm{Im}(\omega)/(2\pi) = 0.4\ \mathrm{ns}^{-1}$, in reasonable agreement with the experimental result shown in the Fig. 3 of the paper.

We also proceed further and examine the response at $B =$ 2.8 and 1.8 T, corresponding to $\nu = 2$ and 3, respectively. Because we expect the momentum q to be independent of B, but l is proportional to the magnetic length that scales as $1/\sqrt{B}$, we obtain in these cases $ql = 0.01$ and 0.012, respectively. Considering that v_p is proportional to ν, see Eq. (9), and using $\sigma_{xx}/\sigma_{xy} = 10^{-3}$, we find the decay times $\mathrm{Im}(\omega)/(2\pi) = 0.74$ and 0.93 ns^{-1}, also in reasonable agreement with the results in Fig. 3 of [68].

Note that the effect of metal electrodes can be straightforwardly included by appropriately modifying the integrand in the definition of Λ (55). When $\sigma_{xx}/(\sigma_{xy}ql') \lesssim 1$, and as long as the distance d of the metal gate from the EMP satisfies $d \gg l'$, we find that one can well estimate the eigenfrequency ω by using the complex-valued length l in (74). In this case, the image charge at the electrodes needs to be included by appropriately adjusting ω_0. For example, for a top gate, we modify the EMP velocity (8) by using the Green's function in (25a) instead of (6).

In Fig. 8(b), we show how the attenuation $\mathrm{Im}(\omega)$, obtained for $\sigma_{xx}/\sigma_{xy} = 10^{-3}$ and $d = 10l'$, varies as a function of the wave vector q (solid lines). Comparing to the dissipation of the EMPs in free space (dashed lines), we observe that the lifetime of the excitations is generally reduced by the interaction with the image charge, in agreement with the analysis of Volkov and Mikhailov [36].

1. *Quality factor of QH resonators*

To conclude this section about dissipation, we now discuss how a finite value of σ_{xx} degrades the performance of the devices. We restrict our analysis to QH materials with abruptly terminated edges and a filling factor $\nu = 1$, and so the conductivity profile (48) is expected to be appropriate, see Appendix A. In particular, we focus on a QH droplet of perimeter L_y and we consider for simplicity an electrostatic configuration that does not break the translational invariance in the y direction, i.e., the direction of propagation of the excess charge density ρ. In this case, the droplet supports plasmonic excitations that satisfy periodic boundary conditions for ρ in y. The periodicity of ρ restricts the allowed values of the wave vector to $q = 2\pi n_q/L_y$, where $n_q \in \mathbb{N}$ is the wave number, and so the EMP eigenfrequency is quantized.

In this paper, we refer to this device as a QH resonator, where the resonant frequency is obtained by evaluating the dispersion relation (7) at $q = 2\pi n_q/L_y$. We remark that a QH resonator differs from conventional microwave resonators, where the electromagnetic field propagates back and forth in the bulk of the material instead of chirally along the perimeter; a QH resonator can be designed to mimic a conventional one by appropriately breaking the translational invariance in the y-direction, see e.g. Fig. 3 of Ref. [15].

In lossy microwave resonators, the resonator frequency $\omega_R \equiv \omega(q = 2\pi n_q/L_y)$ becomes complex-valued. The imaginary part of ω_R is related to the attenuation in the system and is often parametrized by the dimensionless quality factor Q, defined as [16]

$$\omega_R = \omega_0\left(1 + \frac{i}{2Q}\right). \tag{75}$$

To obtain an intuitive equation for Q, we further simplify the fitting formula of the complex-valued eigenfrequency ω discussed in Sec. II C by expanding ω around the real part l_0 of l in (74). The result obtained with this expansion agrees reasonably well with the numerics in the same parameter region for which the use of the complex-valued length l is appropriate, i.e., $\sigma_{xx}/\sigma_{xy} \lesssim ql'$.

With this simplification, the Q factor reduces to

$$Q \approx -\frac{G(l_0, q, 0)}{2l_1 \partial_{l_0} G(l_0, q, 0)} = \frac{1}{2}\frac{\sigma_{xy}}{\sigma_{xx}}\left(\frac{\omega_0 \tau^*}{2\pi}\right)^2, \tag{76}$$

where the timescale τ^* is defined by

$$\tau^* = \frac{1}{v_p}\sqrt{\frac{L_y}{n_q}}(-c_0 4\pi^2 \epsilon_S \partial_{l_0} G(l_0, q, 0))^{-1/2}. \tag{77}$$

Here, τ^* represents the time required for an excitation with velocity v_p to travel for an effective relaxation length given by the geometric mean of the characteristic lengths (in the x and y directions) over which the electric field varies. For example, in the long-wavelength limit and without external electrodes,

$$\tau^* = \frac{1}{v_p}\sqrt{\frac{L_y}{n_q}l'}. \tag{78}$$

Note that $\omega_0\tau^* \propto (L_y)^{-1/2}$, so longer resonators have lower Q. For this reason, the metamaterial construction presented in Ref. [15] is particularly appealing to implement long and low-loss transmission lines.

Also, if we consider a metal gate placed at a distance d from the edge of the QH material, such that $qd \ll 1$, we find that the attenuation of the EMP increases marginally, for example, in the presence of a top gate, the time scale τ^* in Eq. (78) acquires the multiplicative prefactor $\sqrt{1 + l^2/(4d^2)} = 1 + \mathcal{O}(l^2/d^2)$. However, the resonance frequency of the resonator decreases drastically because of the regularization of the $\ln(q)$ singularity in the EMP velocity. This consideration implies that the Q factor is lowered by the electrodes; for example, for a top gate setup, $\omega_0\tau^* \propto \ln(1 + d^2/l_0^2)$, and so Q scales logarithmically with d.

We now compare our result with the literature. For example, in Ref. [43], the authors measured the Q factor in a large QH resonator in GaAs with a perimeter $L_y \approx 1$ mm and with electrostatically defined edges. In this case, the width l' of the EMPs into the bulk is expected to depend on the potential applied to the gates and is typically a few hundreds of nanometers, see e.g. [69]. In particular, let us focus on the cavity of perimeter $L_y = 1.75$ mm, with a resonance frequency of 125 MHz. Using the typical value $l' \approx l = 220$ nm and modeling for simplicity the effect of the different screening gates by a single top gate displaced by an average distance d from the QH material, the resonance frequency can be obtained from Eq. (23) and it is $\omega/(2\pi) =$ 128 MHz when $d/l \approx 8.2$ and $\epsilon_S^* \approx 8.7$. From Eq. (78) and neglecting the correction to τ^* due to the gate, we estimate $Q = 2 \times 10^{-3}\sigma_{xy}/\sigma_{xx}$. If we consider again $\sigma_{xx}/\sigma_{xy} \approx 10^{-3}$, which approximately corresponds to a sheet resistance of 50 Ω, we obtain $Q \approx 2$, in reasonable agreement with the measured values that range from 2 to 7 depending on the temperature of the sample. Note that the Q factor in this case is low because L_y is much larger than the characteristic width l' of the EMP in the bulk direction.

Let us now examine a different case. In particular, we focus on a QH resonator of perimeter $L_y = 35$ μm and wave number $n_q = 1$, with a top gate placed at $d = 3$ μm from the EMP and under the effect of a magnetic field $B = 0.1$ T. The electron density is chosen to have a filling factor $\nu = 1$. In this case, we expect a resonance frequency $\omega_0/(2\pi) \approx 10.5$ GHz and $\tau^* \approx$ 42.4 ns. Considering a diagonal resistivity of a few Ohms per square [48–51], experimentally achievable for a wide range of materials at the mK temperatures required for spin qubit operations, we can use $\sigma_{xx}/\sigma_{xy} = 10^{-4}$, and we obtain $Q \approx 10^3$.

Note that in this calculation, we used a two-dimensional material that could reach the integer QH regime with filling factor $\nu = 1$ at a magnetic field $B = 0.1$ T. For this condition to be valid in GaAs, one requires an extremely low carrier density $\sim 10^9$ cm^{-2}. In more realistic GaAs setups, the filling factor $\nu = 1$ is achieved at B fields of a few tesla; in this case, we observe a reduction of the Q factor, which scales as $\sim B^{-1/2}$ up to a logarithmic correction. In our model, this decrease is related to the B-field dependence of the width of the EMP into the bulk, i.e., $l' \propto l_B \propto 1/\sqrt{B}$; this proportionality is a consequence of the assumed sharpness of the edge.

To improve the Q factor, one can conceive of a GaAs construction with electrostatically defined edges as in Ref. [43]. In this case, the length l' is to good approximation independent of B, and is typically much larger than l_B, ultimately leading to a larger value of Q. For example a QH cavity with $\nu = 1$ with a perimeter of $L_y = 125.7$ μm with a top gate at $d = 5$ μm has a frequency $\omega/(2\pi) \approx 2.4$ GHz and a Q factor $Q \approx 500$. We used here the prefactor $l \approx l' = 220$ nm and $\sigma_{xx}/\sigma_{xy} = 10^{-4}$.

An alternative way to improve Q is to use different kinds of two-dimensional materials that stay in the QH regime at low values of the magnetic field. For example, graphene has a very large cyclotron gap, and it can enter in the QH regime at B fields of few hundreds of millitesla [53–55]. In addition, anomalous quantum Hall materials based on magnetically doped thin films of BiSe compounds are known to support chiral edge excitations also in the absence of an external magnetic field [41,50,51].

These materials are also favorable because lower values of the magnetic field are preferable for coupling to spin qubits, where a large value of B reduces the energy of the higher orbitals and so increases the unwanted coupling between computational and noncomputational subspaces. Additionally, at high magnetic fields, the Zeeman energy becomes inconveniently large and also the lifetime of the qubit is reduced.

Our EMP model is based on the semi-classical system of equations (1), where the physics of the QH material enters via Ohm's law (1c). Consequently, we believe that our results hold qualitatively well also in these more exotic materials, when the appropriate values of the bulk conductivity and cutoff length l are used. Quantum mechanical corrections to this model can be captured by a simple dynamical Hartree mean field theory [45] and are expected to modify the EMP eigenfrequency only quantitatively.

III. COUPLING TO QUBITS

There are several different proposals for coupling QH edge states and solid state qubits, e.g., via tunnel [70] or Coulomb interactions [19]. In this section, we focus on the latter approach, and, in particular, we quantify the electrostatic coupling between the EMPs and semiconductor qubits. The coupling strongly depends on the type of qubit chosen and on its design, in particular qubits with higher susceptibility to the electric field have a larger coupling constant.

Here, for example, we analyze only singlet-triplet (ST) qubits and we consider the setup shown in Fig. 9.

The model of the ST qubit is discussed in detail in Appendix B. The qubit is defined by a double-well potential in the (x, y) plane, where the centers of mass of the two dots are displaced by $2a$ in the x direction with respect to each other. In particular, we consider the quartic potential [71]

$$V_C(x, y) = \frac{m\Omega^2}{2}\left(\left(\frac{x^2 - a^2}{2a}\right)^2 + y^2\right), \tag{79}$$

where m is the effective mass of the material and the frequency Ω quantifies the confinement strength. A magnetic field B is applied in the z direction and an electric field E_0 is applied in the direction parallel to the two wells. E_0 creates a dipole moment between the two dots, which results into a finite detuning energy Δ, i.e., a shift of the zero-point energy of the two dots. The field B modifies the characteristic length l_T over which electrons are confined. This length is given by

$$l_T = \sqrt{\frac{\hbar}{m\Omega_T}}, \tag{80}$$

where we define the Fock-Darwin frequency

$$\Omega_T = \sqrt{\Omega^2 + \frac{\omega_c^2}{4}}, \tag{81}$$

and the cyclotron frequency $\omega_c = eB/m$. Also, we introduce the dimensionless constant

$$\beta = \left(\frac{\omega_c}{2\Omega_T}\right)^2 = \left(1 + \left(\frac{2\Omega}{\omega_c}\right)^2\right)^{-1} \in [0, 1), \tag{82}$$

which parametrizes the ratio of magnetic and harmonic confinement energy.

We consider a strongly depleted regime in which there are only two electrons in the double dot. We then choose as computational states the usual antisymmetric (singlet) and symmetric (triplet) combinations of spins in the two dots; the energy gap between these states is given by the exchange interaction J_{ex}. For simplicity, we also neglect the effects of the spin-orbit coupling and of a magnetic field gradient, and so the singlet and triplet subspaces are decoupled. In this case, J_{ex} is obtained by combining Eqs. (B40), (B19), and (B27) and can vary over a few orders of magnitude for different qubit designs. In the following, we restrict the analysis to the value of the design parameters that guarantee an exchange energy in the microwave domain, i.e., $J_{\mathrm{ex}} \lesssim 15$ GHz.

The center of mass of the qubit is placed at a distance τ from the center of mass of the EMP of a QH resonator of perimeter L_y, see Fig. 9. The QH material is assumed to have a filling factor $\nu = 1$ and we only examine the coupling to the lowest mode of the resonator, with wave number $n_q = qL_y/(2\pi) = 1$. We stress that although for simplicity we restrict ourselves to the analysis a QH resonator made of GaAs, we expect our semiclassical results to hold also for other two-dimensional electron gasses such as graphene and anomalous QH materials. Also, we study the amplitude of the coupling between the qubit and the electric field evaluated in the cross section $y = 0$, shown with orange lines in Fig. 7(a).

Note that τ includes a shift x_0 (50) of the EMP charge density into the bulk of the QH material which is caused by the quantum corrections discussed in Sec. II B and in Appendix A. The length τ is also assumed to be sufficiently large for the tunnel coupling to be unimportant and, for this reason, we only focus on the electrostatic coupling. The inductive coupling between the qubit and the magnetic field arising from

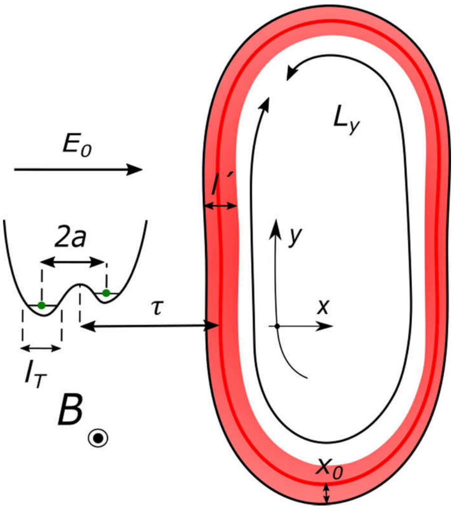

FIG. 9. QH resonator and ST qubit. To define the ST qubit, we consider two electrons in a double dot potential perpendicular to the edge of a QH resonator of perimeter L_y. The two dots are separated by a distance $2a$ and an external electric field E_0 is applied in the direction connecting the dots; the eigenstates of each dot are characterized by a confinement length l_T, see Eq. (80). The QH edge state extends into the bulk for a length $l' = 0.75 l_B$ (49) and its center of mass (red solid line) is at a distance τ from the center of mass of the double dot; τ accounts for the shift $x_0 = 1.15 l_B$ (50) of the EMP charge density into the bulk of the QH material. An homogeneous magnetic field B is applied in the direction perpendicular to the plane.

the current flowing in the transmission line is also neglected. This is justified because the magnetic field generated by the EMP is in the order of few nanotesla, and this results in a coupling strength of a few kHz.

We begin this section by examining the coupling between the ST qubit and the EMP in a lossless QH resonator. We provide a perturbative analysis of the interactions in Sec. III A and a more detailed calculation in Sec. III B. We then consider the lossy resonators described in Sec. II C, and in Sec. III C we discuss the possibility of attaining strong resonator-photon coupling with these systems.

A. Perturbation theory

We now introduce an intuitive model useful to understand qualitatively the Coulomb coupling between EMPs and ST qubits.

First, we remark that in the absence of spin-orbit coupling and magnetic field gradient, an electric field does not couple the singlet and triplet subspaces. For this reason, the qubit dipole moment must be longitudinal, i.e., $\propto \sigma_z$, (σ_z is the Pauli matrix acting on the qubit), and so the resonator-qubit coupling has a form that is desirable for qubit read-out and scalability [56–58].

Also, the qubit dipole moment depends on the externally applied electric field E_0. In particular, from the analysis presented in Appendix B [see Eqs. (B41), (B28), and (B29)], it follows that the nondetuned configuration ($E_0 = 0$) has no dipole moment, and so to the first order of perturbation theory, the qubit is not altered by a homogeneous electric field E. This property can be advantageous because it suppresses charge noise, however it also drastically reduces the electrostatic coupling with transmission lines and resonators.

We discuss here two different procedures that can be followed to circumvent this problem and to obtain a finite photon-qubit interaction.

The first possibility is to use a nonhomogeneous electric field. For example, one can consider an asymmetric structure, where one of the dots experiences a higher electric field than the other [19]. In QH resonators, the electric field decays as $\sim 1/x$ in the direction perpendicular to the edge, see Eq. (A9), and so this asymmetry can be obtained by placing the two dots perpendicularly to the resonator edge, as shown in Fig. 9. In this case, we can obtain a finite coupling also with no external electric field $E_0 = 0$.

To have a simple model that captures the main physics of this device, we Taylor expand the electric field of the EMP in the x direction (perpendicular to the edge) around the center of mass of the qubit, i.e., $E(x) \approx E(0) + \delta E x$, with $\delta E \equiv \partial_x E|_{x\to 0}$, and we study the response of the qubit to the constant electric field gradient δE. We neglect here the spatial variation of the field in the other directions, which in the long-wavelength limit vanishes at the qubit position, see Eq. (A9). If we consider $E_0 = 0$, the homogeneous component of the resonator field has no effect to linear order. In contrast, δE changes the double dot Hamiltonian (B1) by the addition of the quadratic term $-e\delta E x^2/2$ and, to the lowest order in δE, the exchange energy modifies as $J_{\text{ex}} \to J_{\text{ex}} + \delta J_{\text{ex}}$, with

$$\delta J_{\text{ex}} = \chi_t \frac{s}{\sqrt{2}(1-s^2)} a^2 e \delta E. \tag{83}$$

Here, s is the overlap between the ground-state wave functions of the two dots, i.e.,

$$s = e^{-a^2(1+\beta)/l_T^2}, \tag{84}$$

with l_T and β defined in Eqs. (80) and (82), respectively. The prefactor χ_t quantifies the susceptibility of the qubit to a change in the tunnel coupling t between the two dots; χ_t strongly depends on the qubit design. An explicit expression for χ_t is given in Eq. (B42a).

To find the interaction Hamiltonian, we now quantize the electric field of the QH resonator as described in Appendix A 1. Considering, for simplicity, the far field (in the sense of Sec. II) and long-wavelength asymptotic expression of $\mathbf{E}(\mathbf{r})$ in Eq. (A9), we obtain

$$H_{\text{int}} = \frac{\hbar\gamma_1}{2}\sigma_z(\hat{a}^\dagger + \hat{a}), \tag{85}$$

with $\hat{a}$ being the annihilation operator for a single boson in the cavity. The coupling constant γ_1 is given by

$$\frac{\gamma_1}{2\pi} = -\sqrt{2}\frac{v_p}{L_y}\chi_t \frac{s}{1-s^2}\frac{a^2}{\tau^2}; \tag{86}$$

v_p is the characteristic plasmon velocity in Eq. (9) evaluated at the filling factor $\nu = 1$.

To have an estimation of γ_1, let us consider two weakly coupled dots; in this case, Eq. (86) simplifies to

$$\frac{\gamma_1}{2\pi} \approx 2\sqrt{2}\frac{v_p}{L_y}\frac{t}{|U_{\text{Hu}}|}\operatorname{csch}\left(\frac{a^2}{l_T^2}(1+\beta)\right)\frac{a^2}{\tau^2}. \tag{87}$$

The energy U_{Hu} is the on-site Hubbard energy, which quantifies the Coulomb interactions caused by the double occupation of a single dot. We consider the coupling between dots to be weak when U_{Hu} is much greater than all the other energy contributions. As discussed in Appendix B, using the quartic confinement potential (79), one can find explicit expressions of U_{Hu} and of the tunnel energy t as a function of the qubit design parameters (i.e., a, Ω, B). The result is obtained by combining Eqs. (B19), (B25), and (B27).

For example, for a realistic GaAs ($\epsilon_S^* \approx 8.7$) resonator of perimeter $L_y = 20$ μm, the prefactor is $v_p/L_y \approx 2$ GHz; using also $t/|U_{\text{Hu}}| = 0.1$, $a = l_T$, $\tau = 3a$, and $\beta = 0.01$, we obtain $\gamma_1/(2\pi) \approx 53$ MHz, comparable with the coupling strength in a strongly coupled spin-photon system [17,18,32].

It is also interesting to observe that there is a finite coupling to the electric field gradient δE even if the dots are rotated and aligned parallel to the resonator edge. This coupling originates from the different magnetic field dependent phases between the wave functions of the two dots, and its magnitude is reduced, compared to Eq. (86), by the multiplicative factor β in Eq. (82).

The second procedure to obtain a finite coupling in this setup is to move away from the sweet spot that suppresses charge noise and to include a small homogeneous electric field E_0 in the x direction, see Fig. 9. The qubit then acquires a finite dipole moment and it becomes susceptible in the first order to the homogeneous (averaged) component of the electric field of the QH resonator $E(0) \equiv E$ [20]. Note that in this approach, the qubit is more vulnerable to charge noise; however, since E is quite high, one can achieve a finite coupling strength even for small values of E_0, for which the qubit susceptibility to noise is still low.

Combining Eqs. (B41), (B28), and (B29), we find that the correction to J_{ex} linear in E is

$$\delta J_{\text{ex}} = 2e^2\big(\chi_t t_2 + \chi_\Delta \Delta_1^2\big)E_0 E. \tag{88}$$

Here, χ_Δ is defined in Eq. (B42b) and is the susceptibility of the qubit to the detuning Δ. The quantities Δ_1 and t_2 are the coefficients that relate the detuning Δ and the tunnel energy t to the total homogeneous electric field ($E_{\text{tot}} = E_0 + E$), respectively; explicit equations for Δ_1 and t_2 are given in Eq. (B30).

Using Eq. (A9), one obtains a longitudinal interaction Hamiltonian as in Eq. (85), with coupling strength, which we will now call γ_2, given by

$$\frac{\gamma_2}{2\pi} = -4\frac{v_p}{L_y}\big(\chi_t t_2 + \chi_\Delta \Delta_1^2\big)\frac{eE_0}{\tau}. \tag{89}$$

Considering again two weakly coupled dots, γ_2 simplifies to

$$\frac{\gamma_2}{2\pi} \approx -\operatorname{sign}(E_0)6\sqrt{2}\frac{v_p}{L_y}\frac{t}{|U_{\text{Hu}}|}\operatorname{csch}\left(\frac{a^2}{l_T^2}(1+\beta)\right)\frac{b_0}{\tau}, \tag{90}$$

where we introduce the length b_0 defined by

$$b_0 = \frac{e|E_0|}{m\Omega^2}, \tag{91}$$

which characterizes the shift of the single dot wave functions due to the external field E_0, see Eq. (B7).

If we use the same realistic parameters used to estimate γ_1 in Eq. (87), i.e., $L_y = 20\ \mu\text{m}$, $t/|U_{\text{Hu}}| = 0.1$, $a = l_T$, $\tau = 3a$, and $\beta = 0.01$, and we consider the value of E_0 for which $b_0 = 0.1a$, we obtain $\gamma_2/(2\pi) \approx -\operatorname{sign}(E_0)48$ MHz.

Note that a homogeneous electric field in the y-direction only shifts the qubit center of mass and its zero-point energy, and so in the rotated configuration, where the qubit is parallel to the QH edge, we obtain $\gamma_2 = 0$.

Also, we remark that the total coupling γ_{tot} is given by the sum of two contributions of the same order of magnitude, i.e., $\gamma_{\text{tot}} = \gamma_1 + \gamma_2$, one of which is externally tunable because of E_0. For example, by aligning E_0 to the electric field of the resonator (i.e., $E_0 < 0$), the total coupling increases, and for the parameters used, it reaches the value $\gamma_{\text{tot}}/(2\pi) \approx 100$ MHz, while in the opposite limit ($E_0 > 0$), the coupling is minimized. In devices with more qubits coupled to the same resonator, this tunability can be exploited to control selectively the coupling of each individual qubit [72,73].

It is important to notice that both coupling terms are inversely proportional to the perimeter of the resonator L_y, and therefore shorter QH droplets have higher coupling to the qubit. Additionally, as explained in Sec. II C 1, the EMPs in shorter droplets have a higher lifetime, and, consequently, a higher Q factor. We remark again that longer transmission lines can be manufactured from shorter resonators by using the metamaterial construction described in Ref. [15].

To conclude this analysis, we now comment on the effect of metal electrodes on the coupling constant. Because of the electrodes, the electric field of the resonator changes as described in Sec. II B 2; the Coulomb interactions in the double dot are also modified [see Eq. (B19)], but these corrections are negligible. In particular, we consider here only two different configurations: a top and a side gate placed at distance d from the center of mass of the EMP. A top gate decreases the averaged resonator field E in the x-direction, but, when $d > \tau/2$, it increases the electric field gradient δE; for this reason, a top gate is more convenient to increase γ_1. In contrast, a side gate has the opposite effect: it increases E and decreases δE, and so a side gate is advantageous to attain a higher value of γ_2, for which we require a finite E_0. When $d \gg L_y$, the corrections to the electric field caused by the metal are negligible and Eqs. (86) and (89) are appropriate.

B. Hartree integral

The perturbative solution presented in Sec. III A is expected to give a good estimation of the coupling strength in the far-field limit, i.e., when $\tau \gg a, l, l_T$ and $|q|\tau \ll 1$. To verify the validity of Eqs. (86) and (89), we find an effective Hamiltonian capturing the EMP-qubit coupling by computing the Hartree integral

$$H_{\text{int}} = \int d\mathbf{r} \int d\mathbf{r}' \rho_{\text{R}}(\mathbf{r}) G(\mathbf{r}, \mathbf{r}', 0) \rho_{\text{D}}(\mathbf{r}'), \tag{92}$$

and by projecting the result onto the qubit subspace. Here, G is the Green's function of the electrostatic configuration chosen (and evaluated in the $z = 0$ plane), ρ_{R} is the charge density operator of the EMP in the resonator, obtained by selecting the term with the appropriate wave vector $q = 2\pi n_q/L_y$ in Eq. (A8), and ρ_{D} is the charge density of the double dot. We consider again a QH resonator with filling factor $\nu = 1$ and wave number $n_q = 1$. The detailed solution of (92) is presented in Appendix C.

This procedure accounts for the precise spatial profile of the electric field (and of its gradient) and it captures also near-field corrections; the resulting couplings $\gamma_{1,2}$ are given by

$$\frac{\gamma_1}{2\pi} = \frac{v_p}{L_y}\frac{\chi_t s a^2}{\sqrt{2}(1-s^2)}\left(\frac{2g(\tau) - g(\tau - a) - g(\tau + a)}{a^2}\right) \tag{93}$$

and

$$\frac{\gamma_2}{2\pi} = \frac{v_p}{L_y}\big(\chi_\Delta \Delta_1^2 + \chi_t t_2\big) eE_0 \left(\frac{g(\tau + a) - g(\tau - a)}{a}\right). \tag{94}$$

The dimensionless function g depends on the electrostatic configuration considered. In particular, in free space, it is related to the function g_0 [defined in Sec. II B 2 as the projection onto the (x, y) plane of the EMP potential $\mathcal{G}_0$] by the substitution $l' \to \lambda = \sqrt{l'^2 + l_T^2}$, see Eqs. (C8) and (61). When a top (side) gate are included, we have $g = g_0 + g_{t(s)}$. The functions $g_{t,s}$ are given in Ref. (C10) and are obtained by using the substitution $l' \to \lambda$ in the $z = 0$ limit of (66). For simplicity of notation, we have dropped the explicit q dependence in g.

In Fig. 10(a), we show how the coupling γ_1 to the electric field gradient of the QH resonator changes as a function of the distance τ. For the plot, we consider a resonator with a perimeter $L_y = 27.7\ \mu\text{m}$ and two dots very close to each

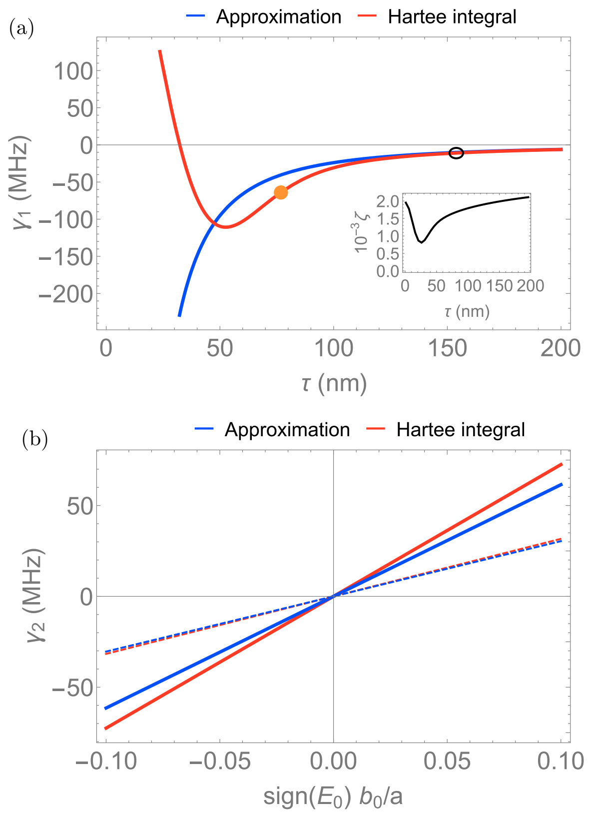

FIG. 10. Coupling constants $\gamma_{1,2}$. For the plots, we use $2a = 30$ nm, $\Omega = 3.85$ meV, $B = 0.44$ T, and $L_y = 27.7\ \mu$m; we consider $l' = 0.75 l_B$ and $x_0 = 1.15 l_B$, as discussed in Sec. II B. We also include the effect of a top gate placed at distance $d = 0.6\ \mu$m from the EMP. In (a), we consider $E_0 = 0$. The blue line is obtained using Eq. (86), and the red line is obtained using Eq. (93). In the inset, we plot the dimensionless parameter ζ, defined in Eq. (C18), which quantifies the coupling between the computational and the noncomputational subspace of the double dot. In (b), we show the dependence of the coupling γ_2 on a homogeneous electric field E_0. The length b_0 is defined in Eq. (91) and it is proportional to $|E_0|$; to include negative values of E_0, we rescale the horizontal axis by sign(E_0). The blue and red lines are obtained respectively by using Eqs. (89) and (94). The solid and dashed lines are obtained by using $\tau = \tau_s = x_0 + a + l_T \approx 77$ nm, and $\tau = 2\tau_s \approx 154$ nm. These values of τ are marked in (a) by using an orange dot and a black circle, respectively.

other, with $2a = 30$ nm. We also consider an harmonic confinement potential $\Omega = 3.85$ meV and an external magnetic field $B = 0.44$ T. For these parameters, the susceptibility to tunneling is $\chi_t \approx 0.8$, and differs only slightly from the weak tunnel coupling expansion $\chi_t^{\text{weak}} \approx -4t/|U_{\text{Hu}}| \approx 0.6$. We also include a top gate at a distance $d = 0.6\ \mu$m, which is required to slow the EMPs, but has no significant effect on the coupling. In this setup, the exchange energy and the resonance frequency of the resonator are both in the microwave domain: in particular, we find $J_{\text{ex}} \approx 12.2$ GHz and $\omega_R \approx 12.6$ GHz, respectively. The resonator frequency ω_R is calculated from the far-field result (7) by using the Green's function (25a) in the EMP velocity (8). The wave vector is $q = 2\pi/L_y$ and the cutoff length is $l \approx 0.75 \times 0.53 l_B$; the two quantitative corrections to the magnetic length originate respectively from the quantum correction (49) and from the spatial profile of the conductivity (59).

Also, the interaction with the resonator causes a finite coupling between the computational and the noncomputational subspace of the double dot. This coupling is quantified by the dimensionless parameter ζ, that is defined in Eq. (C18) and is plotted in the inset of Fig. 10(a). For the qubit designs considered here, we find that ζ is negligible and so the Hamiltonian (85) provides a good description of the system.

From the figure, we observe as expected that the two different approaches used for computing the coupling γ_1, i.e., Eqs. (86) and (93), differ when the qubit is close to the resonator edge, but they coincide in the far field, when $\tau \gg a$. This limiting behavior can be easily understood considering that, except for the different length $l' \to \lambda$ in the definition of g, the combination of functions g with different arguments in the parentheses in Eq. (93) is proportional to the discrete second derivative in x of the EMP potential in the (x, y) plane (60b), and, consequently, to the discrete derivative of the electric field. This function reduces exactly to the continuum value of δE when $a \to 0$. In other words, from a detailed analysis, we find that the simple perturbative result for the exchange energy in Eq. (83) has the correct form, but the continuous gradient δE is replaced by its discrete analog.

More care is required when examining the coupling term γ_2. In this case, in fact, we find that the Hartree integral and the perturbative treatment presented in Sec. III A do not agree quantitatively. In fact, a direct estimation of γ_2 from (92) leads to Eq. (C13). This equation differs from Eq. (89) even in the far-field limit, where the two approaches should coincide. The reason for this disagreement is discussed in detail in Appendix C. To summarize, this difference can be traced back to the explicit dependence on the averaged resonator field E of the Fock-Darwin wave functions in Eq. (B11), which is neglected in the Hartree integral. For this reason, the qubit susceptibility to E obtained by this method differs from the one calculated in Sec. III A, see Eqs. (C16) and (88); the latter equation provides a more accurate estimation of the susceptibility. Because the terms neglected in the Hartree integral are not expected to change the function in parentheses in (C13), which is proportional to the discrete derivative of the EMP potential V, we adjust the prefactor in Eq. (C13) by using the *ad hoc* substitution shown in (C17); with this procedure, we obtain Eq. (94).

In Fig. 10(b), we show the correction to the coupling energy by including a small homogeneous electric field E_0. The parameters used in the plot are the same as in Fig. 10(a) and we select the two different values of τ labeled by an orange and a hollow dot in the figure; both values of τ are large enough to guarantee a negligible overlap between the EMP and the qubit wave function, and so the tunnel coupling is unimportant. After the substitution (C17), we observe that the results are in good agreement in the far field (dashed lines), while they differ slightly in the near field (solid lines). We remark again that γ_1 and γ_2 can be in the same order of magnitude for small E_0, and so, depending on the sign of E_0, the total coupling $\gamma_{\text{tot}} = \gamma_1 + \gamma_2$ can be significantly increased or decreased.

C. Strong EMP-qubit coupling

We can now discuss the possibility of attaining strong coupling between the EMP and the qubit. The coupling is strong when γ is larger than all the losses in the system. The lifetime of ST qubits (in GaAs) is often limited by the dephasing time, which is in the order of 100 ns [74], but this lifetime can be increased up to 200 μs by spin echo [75]. For the relevant frequency range, the estimated EMP lifetime is of the order of $Q/\omega_R \sim 10^3/(1\text{ GHz}) \sim 1\ \mu$s, and so we consider this factor as the limiting timescale and we define the dimensionless ratio Γ of coupling strength and attenuation in the resonator

$$\Gamma \equiv \frac{\gamma}{\mathrm{Im}(\omega_R)}. \tag{95}$$

When $|\Gamma| > 1$, the resonator and the qubit are strongly coupled.

We now restrict our analysis to the case $E_0 = 0$, and we consider the near-field expression of γ_1 in Eq. (93); the values of Γ that we find here can be approximately doubled by a finite E_0. Also, we include a top gate at distance d and we obtain the complex resonator frequency ω_R by combining Eqs. (7), (25a), and (74).

In Fig. 11(a), we show how Γ changes as a function of the perpendicular magnetic field B and of the harmonic confinement strength Ω for two quantum dots that are placed $2a = 30$ nm apart. For the plot, the distance between the qubit and the resonator edge is kept fixed to a minimal value $\tau = \tau_s = x_0 + a + l_T$; also, the resonator has a perimeter $L_y = 27.7\ \mu$m and we choose $d = 0.6\ \mu$m. Note that the resonance frequency of the resonator depends on the magnetic field via the magnetic length; however, this choice of L_y and d guarantees that, for all the values of B considered, the resonator frequency remains in the microwave domain, i.e., $\mathrm{Re}(\omega_R) \lesssim 15$ GHz. Also, in the plot, we highlight the regions of parameters for which the exchange energy J_{ex} takes values outside the microwave domain and we exclude them from the discussion. We observe that there is a large range of values of Ω and B in the allowed region, for which $|\Gamma|$ is greater than one and so strong coupling is indeed possible. As an example, in the figure, we marked with an orange dot the point corresponding to the orange dot in Fig. 10. For this choice of parameters and using the realistic value of diagonal conductivity $\sigma_{xx}/\sigma_{xy} = 10^{-4}$, we obtain $\Gamma \approx -4$.

The ratio Γ can be increased in different ways. For example, one can use high quality QH materials with a lower value of σ_{xx} or one can optimize the configuration of the electrodes to improve the electrostatic coupling [31–33].

Another possibility that can greatly enhance the interaction strength is to modify the qubit design, for example by lowering the harmonic confinement potential Ω. In Fig. 11(a), we observe that by reducing Ω, one can achieve higher values of $|\Gamma|$. To remain in the microwave domain, however, a finer tuning of Ω and B is required. This enhancement is related to the fact that when the value of Ω decreases (and B is low enough to guarantee $\beta \ll 1$), the confinement length l_T increases. Because the susceptibility of the qubit to the electric field (and to its gradient) varies exponentially with $(a/l_T)^2$, the coupling γ can be made significantly larger. In this way, one can achieve strong coupling even in state-of-the-art qubit designs where the two dots are hundreds of nanometers apart.

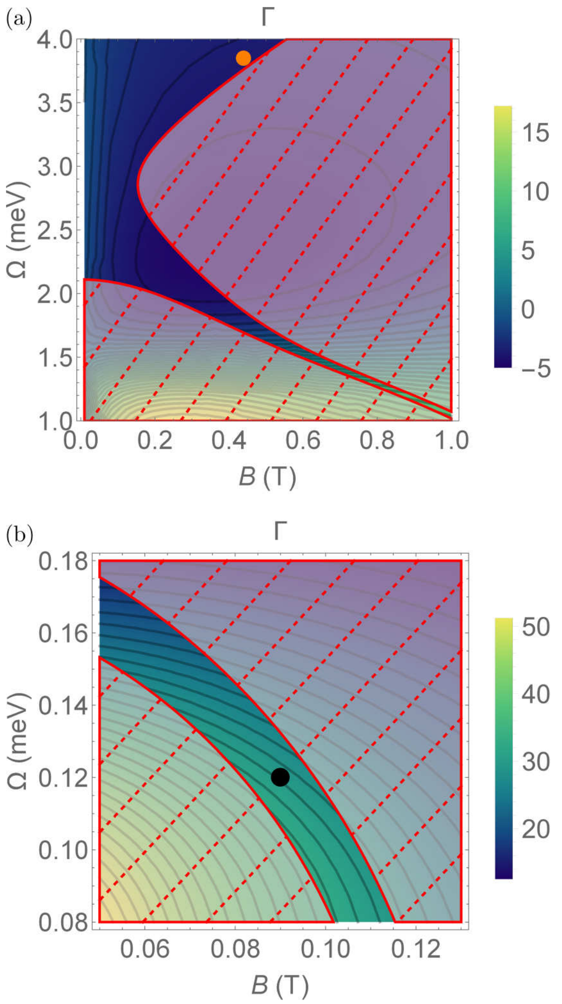

FIG. 11. Ratio Γ of the coupling constant γ_1 and the attenuation of the QH resonator as a function of the magnetic field B and of the harmonic confinement strength Ω. In (a), we consider two dots very close to each other, with $2a = 30$ nm and we include a top gate at distance $d = 0.6\ \mu$m from the system. In (b), we consider two dots $2a = 100$ nm apart and we included a top gate at distance $d = 2.2\ \mu$m. The orange and black dots in (a) and (b) mark the parameters used in Fig. 10 ($B = 0.44$ T and $\Omega = 3.85$ meV) and in Fig. 12 ($B = 90$ mT and $\Omega = 0.12$ meV), respectively. In both figures, we consider a resonator of length $L_y = 27.7\ \mu$m and we place the qubit at a distance $\tau = \tau_s = x_0 + a + l_T$ from the QH edge ($x_0 = 1.15 l_B$). The value of τ_s depends on B and Ω; for the parameters corresponding to the orange (black) point, it is $\tau_s = 77$ nm ($\tau_s = 242$ nm). The regions of parameters marked by red dashed lines are characterized by an exchange coupling outside the microwave domain, i.e., $J_{\mathrm{ex}} > 15$ GHz.

As an example, in Fig. 11(b), we show how Γ changes as a function of Ω and B when the dots are placed at a distance of $2a = 100$ nm. Note that the scale of both Ω and B are reduced by approximately an order of magnitude compared to Fig. 11(a), and, for this reason, in this design a more careful tuning of the parameters is required to remain in the microwave domain. For this plot, we used a resonator of

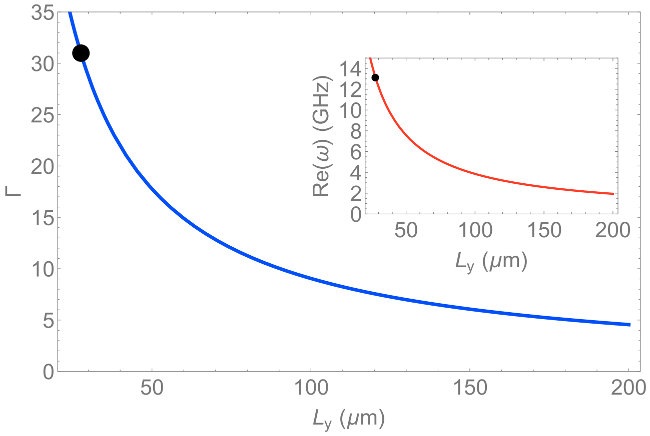

FIG. 12. Ratio Γ of the coupling constant γ_1 to the attenuation of the QH resonator as a function of perimeter of the QH resonator L_y. For the plot, we use $2a = 100$ nm, $d = 2.2$ μm, $\tau = 242$ nm, $B = 90$ mT, and $\Omega = 0.12$ meV. In the inset, we show the dependence of the resonance frequency on L_y. The black dots mark the special value $L_y = 27.7$ μm: for this value of L_y, the value of Γ here is equal to the value marked by the black dot in Fig. 11(b).

perimeter $L_y = 27.7$ μm and a top gate placed $d = 2.2$ μm apart, for which we obtain $\mathrm{Re}(\omega_R) \lesssim 15$ GHz. We observe now values of Γ that are approximately an order of magnitude higher than in Fig. 11(a). In particular, at the point marked by the black dot, i.e., $\Omega = 0.12$ meV and $B = 90$ mT, one obtains $J_{\mathrm{ex}} = -6$ GHz, $\mathrm{Re}(\omega_R) = 13.1$ GHz. When $\tau = \tau_s \approx 240$ nm and $\sigma_{xx}/\sigma_{xy} = 10^{-4}$, the coupling constant is $\gamma_1 \approx 211$ MHz and the quality factor of the resonator is $Q \approx 965$: using these values, one obtains the dimensionless coupling ratio $\Gamma \approx 31$.

We conclude this analysis by briefly discussing the dependence of Γ on the perimeter L_y of the resonator. This dependence is shown in Fig. 12; for the plot we used the parameters marked by the black dot in Fig. 11(b). As expected, Γ decreases approximately as $\sim 1/L_y$ and it has the same scaling as $\mathrm{Re}(\omega_R)$. We observe that, despite this decrease, the coupling remains strong for resonators with a perimeter up to 100 μm long: this property can be exploited to entangle spin qubits over large distances.

IV. CONCLUSIONS AND OUTLOOK

We analyze the physics of QH devices and their coupling to qubits. The electric current in these devices is carried by magnetoplasmonic excitations localized at the edge of the QH material that propagate along the perimeter. By using a semiclassical model capturing the main features of these excitations, we compute the spatial profile of the electromagnetic field in a variety of relevant cases and we justify the phenomenological model used in Ref. [15]. We consider a conductivity tensor which varies from zero to the bulk value over a length l' of the order of the magnetic length. This approach is justified by a quantum mechanical treatment of the EMPs, and, by comparing the results of the two calculations, we extract the value of l'. We also account numerically for the dissipation due to a finite real-valued σ_{xx} and we find a simple fitting formula to estimate the Q factor of the QH resonator.

Using these results, we quantify the Coulomb coupling between EMPs and singlet-triplet qubits. In particular, we discuss two coupling schemes: the coupling to the gradient of the electric field of the resonator and the coupling mediated by an externally applied electric field. For both cases, we find a simple analytic expression that can be used to estimate the coupling strength and we compare it to a more detailed solution based on the computation of the Hartree interaction integral. We find that the coupling strength obtained for the two mechanisms is comparable and so the photon-qubit coupling can be tuned over a wide range of values. Finally, we discuss the possibility of achieving the strong photon-qubit coupling regime by comparing the strength of photon-qubit interaction to the estimated attenuation of the resonator; we conclude that strong photon-qubit coupling is indeed achievable with state-of-the-art qubit designs.

Some effects have been neglected in this analysis that might have an effect on the quantitative value of the interaction strength. For example, the ground-state projection used to derive the double dot Hamiltonian is questionable for certain qubit designs. The neglected terms which mix high orbital states in the two dots, become important when the qubit confinement energy is lowered and thus we expect a quantitative change in the estimated value of the exchange energy and of the susceptibility of the qubit. We believe that the higher orbital states do not change the qualitative picture discussed here, and that including their effect, interaction strengths of 100 MHz and higher can still be reached. Also, we did not include other effects that are relevant for the qubit design such as spin-orbit coupling and magnetic field gradient, which are required to implement qubit gates. These additional terms in the Hamiltonian mix the singlet and triplet sectors, and thus they can potentially lead to some qualitative difference in the interaction strength, and to additional transversal coupling terms $\propto \sigma_{x,y}(\hat{a}^\dagger + \hat{a})$. We believe that these extra terms can be made small by a careful qubit design, but we did not analyze them quantitatively.

ACKNOWLEDGMENTS

The authors would like to thank D. Reilly, A. C. Doherty, A. Ciani, V. Langrock, and F. Hassler for useful discussions. This work was supported by the Alexander von Humboldt foundation.

APPENDIX A: QUANTUM CORRECTIONS

We discuss here the effect of quantum corrections in a QH material with filling factor $\nu = 1$. We assume that the boundary of the QH droplet is atomically defined, and so we neglect the edge reconstruction caused by the static Coulomb interactions [76]. In the long-wavelength limit, the total EMP propagation velocity can be decomposed into a sum of two velocites: an electrostatic term and a quantum correction [44–47]. In a RPA analysis [45], one finds that the former term is proportional to the matrix element of the Coulomb interactions

$$v_c(q) = \frac{e^2}{\hbar} \int dx dx' |\psi_0(x)|^2 G(x - x', q, 0) |\psi_0(x')|^2, \quad \text{(A1)}$$

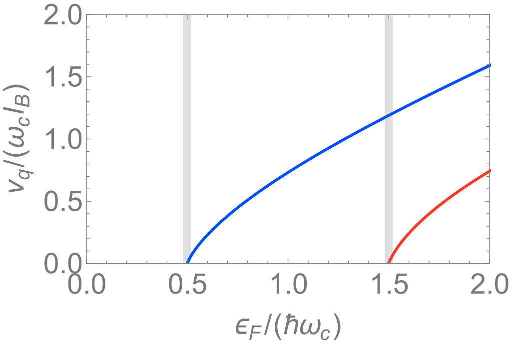

FIG. 13. Quantum velocities as a function of the Fermi energy ϵ_F. The blue and red lines are the quantum velocities associated to the first and second Landau level, respectively.

while the latter is given by the group velocity of a single electron wave packet

$$v_q = \frac{1}{\hbar}\frac{\partial \epsilon_0(k)}{\partial k}. \qquad \text{(A2)}$$

Here, G is the electrostatic Green's function of the electrostatic configuration chosen, e.g. without gate it is given in Eq. (6); $\epsilon_0(k)$ is the band dispersion of the lowest Landau level caused by presence of an edge and ψ_0 is the corresponding single-electron wave function. Both quantities need to be evaluated at the Fermi momentum k_F. Also, in the RPA analysis [45], the EMP charge density is proportional to the absolute value squared of the single electron wave function, i.e., $\rho \propto |\psi_0(x)|^2$.

To estimate these velocities, we can use the model Hamiltonian $H = \boldsymbol{\pi}^2/(2m)$ and impose the boundary condition of vanishing wave function at $x = 0$. Here, m is the effective mass of the QH material and $\boldsymbol{\pi} = \mathbf{p} + e\mathbf{A}$ is the dynamical momentum ($\mathbf{p} = -i\hbar\nabla$ is the canonical momentum and $\mathbf{A}$ is the vector potential). The eigensystem in the Landau gauge is [45]

$$\Psi_0(\mathbf{r}) = Ce^{iky}\psi_0(x), \qquad \text{(A3a)}$$

$$\psi_0(x) = e^{-\frac{1}{2}\left(\frac{x}{l_B}+kl_B\right)^2} H_{\xi_0(k)}\left(\frac{x}{l_B}+kl_B\right), \qquad \text{(A3b)}$$

$$\epsilon_0(k) = \hbar\omega_c\left(\xi_0(k)+\frac{1}{2}\right), \qquad \text{(A3c)}$$

where $H_{\xi_0(k)}$ are the Hermite functions, C is a normalization constant, $\omega_c = eB/m$ is the cyclotron frequency and $l_B = \sqrt{\hbar/(eB)}$ is the magnetic length. We defined the monotonic function $\xi_0(k)$, which is the lowest solution of the dispersion relation

$$H_{\xi_n(k)}(kl_B) = 0. \qquad \text{(A4)}$$

Note that by imposing $\nu = 1$, we are restricting the possible values of the Fermi energy to a fixed interval, i.e., $\epsilon_F/(\hbar\omega_c) \in (1/2, 3/2)$.

The quantum contribution to the velocity can be now estimated from Eq. (A3c) and it can be expressed in terms of the Fermi energy ϵ_F by inverting the function ξ_0; the results are shown in Fig. 13. The characteristic scales of quantum and electrostatic velocities in GaAs are comparable, $\omega_c l_B \approx 7.2 \times 10^4\sqrt{B/\,\mathrm{T}}$ m/s, $v_p \approx 4 \times 10^4$ m/s, however their prefactors usually differ by an order of magnitude because of the $\ln(q)$ divergence of v_c. The presence of a metal electrode reduces v_c leaving v_q approximately unchanged and so the two velocities become comparable. However, even in this case, we do not expect the quantum corrections to modify the qualitative picture as long as $d \gg l_B$ and so, for simplicity, we neglect them in the text.

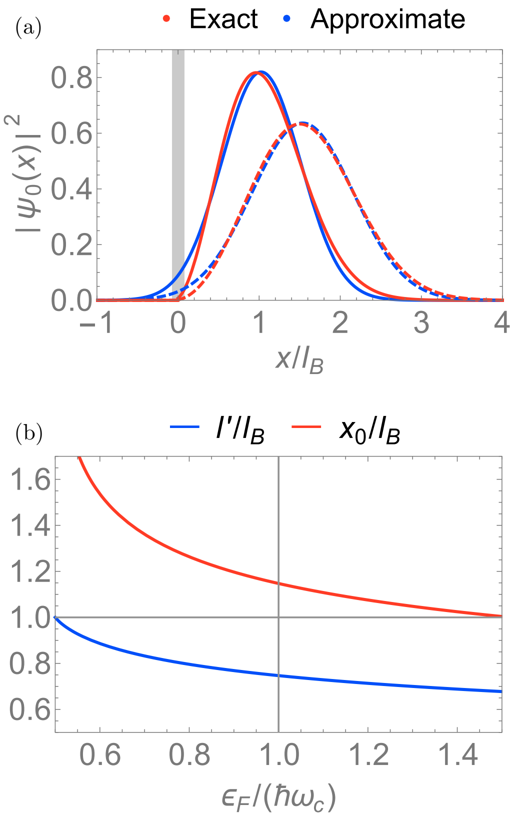

FIG. 14. (a) Comparison between the exact wave functions in Eq. (A3b) (red lines) and the normalized and shifted gaussian in Eq. (A5) (blue lines). We used $\epsilon_F = 1.4\hbar\omega_c$ for the solid lines and $\epsilon_F = 0.6\hbar\omega_c$ for the dashed lines. The thick gray line indicates the physical edge of the QH material. (b) Fitting parameters l' (blue line) and x_0 (red line) in units l_B as a function of the Fermi energy ϵ_F.

The eigenfunctions in Eq. (A3b) are shifted gaussians weighted by Hermite functions. In the regime considered, where ϵ_F is relatively close to the lowest Landau level, the corrections due to the Hermite functions are small and we approximate $|\psi_0(x)|^2$ by a normalized gaussian, i.e.,

$$|\psi_0(x)|^2 \approx \frac{e^{-(x-x_0)^2/l'^2}}{\sqrt{\pi}l'}, \qquad \text{(A5)}$$

where the shift x_0 and the broadening l' are both of the order of the magnetic length. Note that in RPA, the EMP charge density is $\rho \propto |\psi_0(x)|^2$ [45,46], so this form of ρ is consistent with the results obtained with the semiclassical analysis presented in Sec. II B.

Figure 14(a) shows a comparison between the gaussian approximation and the exact wave function in Eq. (A3b); in Fig. 14(b) we also show the dependence of the fitting parameters l' and x_0 on the Fermi energy. In our analysis, we fix the Fermi energy to the middle of the Landau level gap, and so we use $l' \approx 0.75 l_B$ and $x_0 \approx 1.15 l_B$.

Also, note that using the charge density in Eq. (A5), the integral in Eq. (A1), which defines the electrostatic velocity, can be computed analytically, leading to

$$\frac{v_c}{v_p} = e^{-\frac{(ql')^2}{4}} K_0\left(\frac{(ql')^2}{4}\right) = -\ln\left(\frac{(ql')^2 e^{\gamma}}{8}\right) + \mathcal{O}((ql')^2), \tag{A6}$$

in agreement with Eq. (58).

1. Quantization of the EMPs

Once the EMP eigenfrequency and spatial profile are known, one can use standard bosonization procedure to obtain the quantum mechanical operator [44,47,77]. In particular, considering only the fastest EMP mode, the Hamiltonian of the QH system reduces to the usual sum of harmonic oscillators

$$H_R = \sum_{q>0} \hbar\omega(q)\left(\hat{a}_q^\dagger \hat{a}_q + \frac{1}{2}\right), \tag{A7}$$

where the resonance frequencies $\omega(q)$ at different wave vectors are approximately given by Eq. (58), and the bosonic ladder operators satisfy the canonical commutation relations $[\hat{a}_{q'}, \hat{a}_q^\dagger] = \delta_{q,q'}$.

The EMP charge density can also be expressed in terms of these bosonic operators [60]. Neglecting quantum corrections that mix monopole and acoustic modes [47] and using the RPA solution for the EMP charge density (consistent with the analysis in Sec. II B), we obtain

$$\rho(\mathbf{r}) = -e|\psi_0(x)|^2 \sum_{q>0} \sqrt{\frac{q}{2\pi L_y}} (e^{iqy}\hat{a}_q^\dagger + e^{-iqy}\hat{a}_q), \tag{A8}$$

with $|\psi_0(x)|^2$ defined in Eq. (A5).

Comparing Eqs. (60a) and (A8), we find that for a fixed resonator perimeter $L_y = 2\pi n_q/q$ (with n_q being the wave number), the two equations coincide if $\rho_0 e^{iqy} \rightarrow -eq(e^{iqy}\hat{a}_q^\dagger + e^{-iqy}\hat{a}_q)/\sqrt{n_q}$. Using this result, one can quickly derive the quantum mechanical operators from the classical analysis in Sec. II B 1. For example, the electric field operator of the resonator in the far-field limit and without electrodes is

$$\mathbf{E}(\mathbf{r}) = \frac{e\sqrt{n_q}}{2\pi\epsilon_S L_y} \begin{pmatrix} \frac{-x}{x^2+z^2} \\ 0 \\ \frac{-z}{x^2+z^2} \end{pmatrix} (e^{iqy}\hat{a}_q^\dagger + e^{-iqy}\hat{a}_q). \tag{A9}$$

Note that the characteristic scale of the electric field can be rewritten in terms of v_p as $\frac{e}{2\pi\epsilon_S L_y} = \frac{h v_p}{e\nu L_y}$, with ν being the filling factor.

APPENDIX B: QUBIT MODEL

1. Double dot Hamiltonian

We now present the model adopted to describe the singlet-triplet qubit shown in Fig. 9. Our derivation follows closely Ref. [71].

We begin by considering the Hamiltonian H_D of a collection of N_e electrons with charge $-e$ (with $e > 0$) and effective mass m confined in the double-dot potential V_C defined in Eq. (79), and under the effect of a constant magnetic and electric field ($\mathbf{B}$ and $\mathbf{E}$, respectively). H_D can be decomposed into a sum of three terms

$$H_D = \sum_{i=1}^{N_e} \left(H_Z(\mathbf{r}_i) + H_O(\mathbf{r}_i) + \sum_{j\neq i} U_{\text{int}}(\mathbf{r}_i, \mathbf{r}_j)\right). \tag{B1}$$

The Zeeman Hamiltonian H_Z splits the energy of spin up and down electrons and it is given by

$$H_Z(\mathbf{r}_i) = -\frac{\hbar\mu g}{2}\mathbf{B}\cdot\boldsymbol{\sigma}_i, \tag{B2}$$

where μ is the Bohr magneton and g is the g-factor; $\boldsymbol{\sigma}_i$ is the vector of Pauli matrices acting on the spin of the ith electron.

The orbital component H_O can be written in the following way:

$$H_O(\mathbf{r}_i) = \frac{\boldsymbol{\pi}_i^2}{2m} + \phi(\mathbf{r}_i) + V_C(\mathbf{r}_i). \tag{B3}$$

Here, $\boldsymbol{\pi}_i$ is the dynamical momentum of the ith electron $\boldsymbol{\pi}_i = \mathbf{p}_i + e\mathbf{A}(\mathbf{r}_i)$, and $\mathbf{A}$ is the vector potential; ϕ is the scalar potential and for constant $\mathbf{E}$ field it reduces to $\phi(\mathbf{r}_i) = -e\mathbf{E}\cdot\mathbf{r}_i$. Also, we consider $\mathbf{E} = E\hat{e}_x$ and $\mathbf{B} = B\hat{e}_z$; E is the total (homogeneous) electric field in the direction connecting the dots, and so it is the sum of the resonator field and the externally applied field.

The Coulomb interactions between the electrons are included in the term $U_{\text{int}}(\mathbf{r}_i, \mathbf{r}_j)$, that can be estimated by

$$U_{\text{int}}(\mathbf{r}_i, \mathbf{r}_j) = \frac{e^2}{2} G(\mathbf{r}_i, \mathbf{r}_j), \tag{B4}$$

with $G(\mathbf{r}_i, \mathbf{r}_j)$ being the electrostatic Green's function for the configuration considered, potentially including the screening effect due to the image charge at the electrodes.

2. Single dot basis

A convenient basis for the problem is provided by the eigenstates of the single-particle Hamiltonian

$$h_\pm = \frac{\boldsymbol{\pi}^2}{2m} - eEx + \frac{m\Omega^2}{2}((x \pm a)^2 + y^2). \tag{B5}$$

The Hamiltonians $h_\pm$ are related to the well-known Fock-Darwin Hamiltonian

$$h_0 = \frac{\boldsymbol{\pi}^2}{2m} + \frac{m\Omega^2}{2}(x^2 + y^2) \tag{B6}$$

by a magnetic translation in the x direction, i.e.,

$$h_\pm = T_B^x(\pm a - b) h_0 T_B^x(\mp a + b) + eE(\pm a - b/2), \tag{B7}$$

where

$$T_B^x(X) = e^{iX(y/l_B^2 + \pi_x/\hbar)} \tag{B8}$$

is the magnetic translation operator that shifts only the scalar potential, leaving the kinetic energy invariant, see, e.g., Ref. [78]. Here, $l_B = \sqrt{\hbar/(eB)}$ is the magnetic length and we introduce the electric length $b = eE/(m\Omega^2)$, see Eq. (91).

We now fix the vector potential and we work in the symmetric gauge $\mathbf{A} = (-By/2, Bx/2, 0)$. The eigenstates of h_0 are easily found by introducing the bosonic ladder operators

$$\alpha_\pm = -il_T\frac{\pm p_y + ip_x}{2\hbar} - \frac{\pm y + ix}{2l_T} \tag{B9}$$

and realizing that in terms of these operators h_0 is simply a sum of independent harmonic oscillators

$$h_0 = \hbar\omega_+\left(\alpha_+^\dagger\alpha_+ + \tfrac{1}{2}\right) + \hbar\omega_-\left(\alpha_-^\dagger\alpha_- + \tfrac{1}{2}\right), \tag{B10}$$

with frequencies $\omega_\pm = \Omega_T(1 \pm \sqrt{\beta})$. The Fock-Darwin frequency Ω_T, its related oscillator length l_T, and the ratio β are defined by Eqs. (81), (80), and (82), respectively.

The eigenfunctions of $h_\pm$ can then be easily constructed from

$$\Psi^\pm_{n_+n_-} = T^x_B(\pm a - b)\frac{(\alpha_+^\dagger)^{n_+}(\alpha_-^\dagger)^{n_-}}{\sqrt{n_+!n_-!}}\Psi_{00}, \tag{B11}$$

where the ground-state wave function of h_0 is the normalized gaussian

$$\Psi_{00} = \frac{e^{-(x^2+y^2)/(2l_T^2)}}{\sqrt{\pi}l_T}. \tag{B12}$$

Explicitly, the ground state of $h_\pm$ has energy

$$\epsilon^\pm_{00} = \hbar\Omega_T + eE(\pm a - b/2) \tag{B13}$$

and its wave function is, up to an overall phase,

$$\Psi^\pm_{00} = \frac{e^{\pm i\sqrt{\beta}ay/l_T^2}}{\sqrt{\pi}l_T}e^{-(y^2+(x-b\pm a)^2)/(2l_T^2)}. \tag{B14}$$

The first excited states are the states with $n_+ = n_- - 1 = 0$ and their energy gap with respect to the ground state is $\Delta\epsilon = \hbar\Omega_T(1 - \sqrt{\beta})$. In strongly confined double dots, where the confinement potential Ω is the dominant energy scale and $\beta \ll 1$, this energy gap is large, and so we can project the problem onto the ground state and neglect mixing to higher orbital states [71].

We use Greek letters to indicate the matrix elements in this shifted Fock-Darwin basis, i.e., Ψ^α_{00}, with $\alpha \in (-, +)$. The matrix elements of the orbital Hamiltonian in Eq. (B3) are

$$H_O^{\alpha\beta} = \begin{pmatrix} \eta_- & \eta_{-+} \\ \eta_{-+} & \eta_+ \end{pmatrix}, \tag{B15}$$

where we define

$$\eta_\mp = \hbar\Omega_T f(a \pm b) - eEl_T\left(\frac{b}{2} \pm a\right), \tag{B16a}$$

$$\eta_{-+} = e^{-a^2(1+\beta)/l_T^2}\left(\hbar\Omega_T f(b) - eEl_T\left(a + \frac{b}{2}\right)\right), \tag{B16b}$$

and the function

$$f(x) = 1 + \frac{3}{8}(1-\beta)\left(\frac{l_T^2}{4a^2} - \frac{a^2}{l_T^2} - 1\right) + (1-\beta)\frac{x}{l_T}\left(\frac{a}{l_T} + \frac{3}{8}\frac{x}{l_T}\left(\frac{l_T^2}{a^2} + \frac{x^2}{3a^2} - 2\right)\right). \tag{B17}$$

Note that in this section, we use an unfortunate notation because the letter β is used to label the dots and to parametrize the ratio of harmonic and magnetic confinement strength, defined in Eq. (82); however, the meaning of β is apparent from the context.

In the Fock-Darwin basis, the matrix elements of the interaction Hamiltonian in Eq. (B4), have some symmetry, in particular, for any $\alpha, \beta \in (-, +)$, such that $\alpha \neq \beta$, the following relations are true:

$$\langle\alpha, \alpha|U_{\text{int}}|\alpha, \alpha\rangle \equiv V_{\text{Hu}}, \tag{B18a}$$

$$\langle\alpha, \alpha|U_{\text{int}}|\beta, \beta\rangle \equiv V_{\text{Ad}}, \tag{B18b}$$

$$\langle\alpha, \beta|U_{\text{int}}|\beta, \alpha\rangle \equiv V_{\text{Ha}}, \tag{B18c}$$

$$\langle\alpha, \beta|U_{\text{int}}|\alpha, \beta\rangle \equiv V_{\text{Fo}}, \tag{B18d}$$

$$\langle\alpha, \alpha|U_{\text{int}}|\alpha, \beta\rangle = \langle\alpha, \alpha|U_{\text{int}}|\beta, \alpha\rangle \equiv V_{\text{M}}. \tag{B18e}$$

Explicitly, the interaction elements are

$$\frac{V_{\text{Hu}}}{\hbar v_p/l_T} = \sqrt{2\pi^3} - \frac{\pi}{d}, \tag{B19a}$$

$$\frac{V_{\text{Ad}}}{\hbar v_p/l_T} = e^{-2a^2(1+\beta)}\left(\sqrt{2\pi^3} - \frac{\pi}{d}\right), \tag{B19b}$$

$$\frac{V_{\text{Ha}}}{\hbar v_p/l_T} = \sqrt{2\pi^3}e^{-a^2}I_0(a^2) - \frac{\pi}{d}, \tag{B19c}$$

$$\frac{V_{\text{Fo}}}{\hbar v_p/l_T} = \sqrt{2\pi^3}e^{-a^2(2+\beta)}I_0(\beta a^2) - e^{-2a^2(1+\beta)}\frac{\pi}{d}, \tag{B19d}$$

$$\frac{V_{\text{M}}}{\hbar v_p/l_T} = \sqrt{2\pi^3}e^{-a^2(5+3\beta)/4}I_0\left(\frac{1-\beta}{4}a^2\right) - e^{-a^2(1+\beta)}\frac{\pi}{d}. \tag{B19e}$$

Here, the lengths a and d are in units l_T, I_0 is the modified Bessel function of the first kind, v_p is defined in Eq. (9) and it has to be evaluated at the filling factor $\nu = 1$. We include the lowest order correction in l_T/d due to the presence of an ideal metal gate at a distance d from the double dot; also we consider $a, b \ll d$ so that the exact position of the gate (i.e., if it is on the side or at the top of the qubit) does not matter.

3. Orthonormal basis and second quantization

The basis states $\Psi^\pm_{00}$ are not orthonormal, and thus the overlap matrix $S_{\alpha\beta} = \langle\Psi^\alpha_{00}|\Psi^\beta_{00}\rangle$ is not the identity. In general, an orthonormal basis $|O\rangle$ can be constructed by applying a linear transformation P to the nonorthonormal states $|NO\rangle$, i.e.,

$$|O\rangle = |NO\rangle P. \tag{B20}$$

Any single-particle operator A transforms from one basis to another according to

$$A_O = P^{-1}S^{-1}A_{NO}S^{-1}(P^{-1})^\dagger. \tag{B21}$$

The transformation P can be found by requiring that the identity operator in the orthonormal basis transforms into the overlap matrix in the nonorthonormal basis, and so we obtain

$$S = (P^{-1})^\dagger P^{-1}, \tag{B22}$$

and the transformation rule modifies as

$$A_O = P^\dagger A_{NO} P = \sum_{\alpha\beta} P^\dagger_{i\alpha} A^{\alpha\beta}_{NO} P_{\beta j}. \tag{B23}$$

For two-particle operators B, the transformation straightforwardly generalizes as

$$B^{ijkl}_O = \sum_{\alpha\beta\gamma\delta} P^\dagger_{i\alpha} P^\dagger_{j\beta} B^{\alpha\beta\gamma\delta}_{NO} P_{\gamma k} P_{\delta l}. \tag{B24}$$

In the following, we use Roman letters to indicates matrix elements in the orthonormal basis.

If we also require P to be an Hermitian matrix, i.e., $P = P^\dagger$, we obtain from Eq. (B22) that $P = S^{-1/2}$. Then, in our case, P reduces to the symmetric real matrix

$$P = \frac{1}{2}\begin{pmatrix} \frac{1}{\sqrt{1+s}} + \frac{1}{\sqrt{1-s}} & \frac{1}{\sqrt{1+s}} - \frac{1}{\sqrt{1-s}} \\ \frac{1}{\sqrt{1+s}} - \frac{1}{\sqrt{1-s}} & \frac{1}{\sqrt{1+s}} + \frac{1}{\sqrt{1-s}} \end{pmatrix}, \tag{B25}$$

with s being the overlap of the ground-state wave functions of the two dots defined in Eq. (84).

Now that we have an orthonormal basis, we can introduce the associated fermionic operators $c_{i\sigma}$, where $i, j, k, l = (-, +)$ labels the position of the dot $x = \mp a$ and $\sigma, \sigma' = (\uparrow, \downarrow)$ labels the spin. We then rewrite the double dot Hamiltonian in Eq. (B1) in the second quantized form

$$H_D = \sum_{i,\sigma\sigma'} H_Z^{\sigma\sigma'} c^\dagger_{i\sigma} c_{i\sigma'} + \sum_{ij,\sigma} H_O^{ij} c^\dagger_{i\sigma} c_{j\sigma} + \frac{1}{2} \sum_{ijlm,\sigma\sigma'} V^{ijkl}_{\text{int}} c^\dagger_{i\sigma} c^\dagger_{j\sigma'} c_{k\sigma'} c_{l\sigma}. \tag{B26}$$

Here, $H_Z = -\frac{\hbar\mu g}{2} B\tau_z$ (τ_i is the ith Pauli matrix acting on the spin degree of freedom) and the matrix elements of H_O (V^{ijkl}_{int}) are found by applying the transformation rules in Eq. (B23) [Eq. (B24)] to the nonorthogonal matrix elements in Eq. (B15) [Eq. (B19)] with P given in Eq. (B25). In particular, we define, with $i \neq j$

$$U_{\text{Hu}} = \sum_{\alpha\beta\gamma\delta} P_{i\alpha} P_{i\beta} V^{\alpha\beta\gamma\delta}_{\text{int}} P_{\gamma i} P_{\delta i}, \tag{B27a}$$

$$U_{\text{Ad}} = \sum_{\alpha\beta\gamma\delta} P_{i\alpha} P_{i\beta} V^{\alpha\beta\gamma\delta}_{\text{int}} P_{\gamma j} P_{\delta j}, \tag{B27b}$$

$$U_{\text{Ha}} = \sum_{\alpha\beta\gamma\delta} P_{i\alpha} P_{j\beta} V^{\alpha\beta\gamma\delta}_{\text{int}} P_{\gamma j} P_{\delta i}, \tag{B27c}$$

$$U_{\text{Fo}} = \sum_{\alpha\beta\gamma\delta} P_{i\alpha} P_{j\beta} V^{\alpha\beta\gamma\delta}_{\text{int}} P_{\gamma i} P_{\delta j}, \tag{B27d}$$

$$t = \sqrt{2} \sum_{\alpha\beta} P_{i\alpha} H^{\alpha\beta}_O P_{\beta j} + \sqrt{2} \sum_{\alpha\beta\gamma\delta} P_{i\alpha} P_{i\beta} V^{\alpha\beta\gamma\delta}_{\text{int}} P_{\gamma i} P_{\delta j}, \tag{B27e}$$

$$\epsilon_I = \frac{1}{2} \sum_{\alpha\beta} \left(P_{-\alpha} H^{\alpha\beta}_O P_{\beta-} + P_{+\alpha} H^{\alpha\beta}_O P_{\beta+}\right), \tag{B27f}$$

$$\Delta = \frac{1}{2} \sum_{\alpha\beta} \left(P_{-\alpha} H^{\alpha\beta}_O P_{\beta-} - P_{+\alpha} H^{\alpha\beta}_O P_{\beta+}\right). \tag{B27g}$$

Each energy contribution has a clear physical meaning. U_{Hu} and U_{Ad} are respectively the on-site and off-site Hubbard terms that quantify the on-site and off-site Coulomb interaction energy due to a double occupation of the dots. The energies U_{Ha} and U_{Fo} are respectively the Hartree and Fock (exchange) contributions of the Coulomb interactions. Furthermore, t is a tunneling energy between the two dots and it includes a small renormalization due to the Coulomb interactions. Δ is the detuning energy and is related to the dipole moment of the homogeneous electric field in the direction connecting the dots, which raises the ground-state energy of one of the dots compared to the other.

It is important to remark that an external electric field E only influences the orbital matrix elements ϵ_I, t and Δ. The dipole energy Δ vanishes when no electric field is applied, and explicitly it has the form

$$\Delta = \Delta_1 eE + \mathcal{O}(eE)^3, \tag{B28}$$

while the tunneling energy can be written as

$$t = t_0 + t_2(eE)^2 + \mathcal{O}(eE)^4. \tag{B29}$$

The corrections to the lowest order in the electric field are given by

$$\Delta_1 = \frac{1}{\sqrt{1-s^2}} \frac{l_T^2}{4a}\left(3 - 4\frac{a^2}{l_T^2}\right), \tag{B30a}$$

$$t_2 = -\frac{3 l_T^2}{4\hbar\Omega_T \sqrt{2}(1-\beta)} \operatorname{csch}\left(\frac{a^2}{l_T^2}(1+\beta)\right). \tag{B30b}$$

4. Singlet-triplet Hamiltonian

We now restrict the analysis to the two-electron sector. A convenient basis to write the Hamiltonian is then the singlet and triplet basis, defined as

$$|S, \mp\rangle = c^\dagger_{\mp\uparrow} c^\dagger_{\mp\downarrow} |0\rangle, \tag{B31a}$$

$$|T, \uparrow\downarrow\rangle = c^\dagger_{-\uparrow\downarrow} c^\dagger_{+\uparrow\downarrow} |0\rangle, \tag{B31b}$$

$$|(S, T), 0\rangle = \frac{c^\dagger_{-\uparrow} c^\dagger_{+\downarrow} \mp c^\dagger_{-\downarrow} c^\dagger_{+\uparrow}}{\sqrt{2}} |0\rangle. \tag{B31c}$$

The singlet states $|S, \mp\rangle$ are the states where two electrons with opposite spin occupy the same dot centered at position $x = \mp a$, the triplet states $|T, \uparrow\downarrow\rangle$ are the states where electrons in different dots have their spin aligned in the direction of the arrow, and the states $|S, 0\rangle$ and $|T, 0\rangle$ are the antisymmetric and symmetric combinations of spins in the two dots, respectively. We use the following ordering of the states:

$$(|S, -\rangle, |S, +\rangle, |S, 0\rangle, |T, \uparrow\rangle, |T, \downarrow\rangle, |T, 0\rangle)^T. \tag{B32}$$

When the effects of spin-orbit coupling and of a magnetic field gradient are neglected, the singlet-triplet decomposition guarantees that the two-electron Hamiltonian is block diagonal,

$$H_D = H_S \oplus H_T. \tag{B33}$$

Using the Wick theorem and subtracting $2\epsilon_I$ to all the diagonal terms, the two blocks are given by

$$H_S = \begin{pmatrix} U_{\text{Hu}} + 2\Delta & U_{\text{Ad}} & t \\ U_{\text{Ad}} & U_{\text{Hu}} - 2\Delta & t \\ t & t & U_{\text{Ha}} + U_{\text{Fo}} \end{pmatrix} \tag{B34}$$

and

$$H_T = \begin{pmatrix} U_{\text{Ha}} - U_{\text{Fo}} + U_Z & 0 & 0 \\ 0 & U_{\text{Ha}} - U_{\text{Fo}} - U_Z & 0 \\ 0 & 0 & U_{\text{Ha}} - U_{\text{Fo}} \end{pmatrix}. \tag{B35}$$

The energy contributions in the singlet sector H_S are given in Eq. (B27). In the triplet sector H_S, we also define the Zeeman energy $U_Z = -\hbar\mu g B$, which separates in energy the $|T, \uparrow\downarrow\rangle$ states because of the applied B field. U_{Fo} is particularly important for ST qubits because it splits the energy of the singlet and triplet states $|(S, T), 0\rangle$ with vanishing angular momentum and it allows to use these states as a qubit basis.

It is important to remark here that the block Hamiltonians (B34) and (B35) are obtained by restricting the total Hilbert space to the subsector spanned by the ground state of each dot [71]. We expect this approximation to hold quantitatively in strongly confined quantum dots, where the energy splitting between the ground and first excited state is higher than the on-site Hubbard energy U_{Hu}; even if this condition is not fulfilled, we believe this model still provides a qualitative understanding of the system.

The triplet sector is already diagonal in this basis, while the singlet eigenstates $(|\tilde{S}, -\rangle, |\tilde{S}, +\rangle, |\tilde{S}, 0\rangle)^T$ are obtained by a unitary rotation $M_S^\dagger$ of the singlet basis $(|S, -\rangle, |S, +\rangle, |S, 0\rangle)^T$. M_S is the matrix of normalized column eigenvectors of H_S.

When no in-plane electric field is applied, i.e., $E = 0$, there is no dipole moment between the two dots and $\Delta = 0$. In this situation, M_S has the simple form

$$M_S = \begin{pmatrix} -\frac{1}{\sqrt{2}} & A(\epsilon_2) & A(\epsilon_0) \\ \frac{1}{\sqrt{2}} & A(\epsilon_2) & A(\epsilon_0) \\ 0 & B(\epsilon_2) & B(\epsilon_0) \end{pmatrix}, \tag{B36}$$

where we introduced the functions

$$A(x) = \frac{2U_{\text{Ha,Fo}} - x}{\sqrt{4t^2 + 2(2U_{\text{Ha,Fo}} - x)^2}} \tag{B37a}$$

$$B(x) = -\text{sign}(t)\sqrt{1 - 2A(x)^2}. \tag{B37b}$$

In this case, the eigenenergies ϵ_i are given by

$$\epsilon_0 = U_{\text{Hu,Ad}} + U_{\text{Ha,Fo}} - \sqrt{2t^2 + (U_{\text{Hu,Ad}} - U_{\text{Ha,Fo}})^2}, \tag{B38a}$$

$$\epsilon_1 = U_{\text{Hu}} - U_{\text{Ad}}, \tag{B38b}$$

$$\epsilon_2 = U_{\text{Hu,Ad}} + U_{\text{Ha,Fo}} + \sqrt{2t^2 + (U_{\text{Hu,Ad}} - U_{\text{Ha,Fo}})^2}, \tag{B38c}$$

where we defined the combination of the Coulomb interaction energies

$$U_{\text{Hu,Ad}} = \frac{U_{\text{Hu}} + U_{\text{Ad}}}{2}, \tag{B39a}$$

$$U_{\text{Ha,Fo}} = \frac{U_{\text{Ha}} + U_{\text{Fo}}}{2}. \tag{B39b}$$

The computational basis is usually defined by the singlet-triplet states $(|\tilde{S}, 0\rangle, |T, 0\rangle)^T$; the energy gap between these states is

$$J_{\text{ex}} = 2U_{\text{Fo}} + U_{\text{Hu,Ad}} - U_{\text{Ha,Fo}} - \sqrt{2t^2 + (U_{\text{Hu,Ad}} - U_{\text{Ha,Fo}})^2}. \tag{B40}$$

This energy gap is often called exchange energy, because in the limit of weakly coupled dots, where $t, U_{\text{Ha,Fo}} \ll U_{\text{Hu,Ad}}$, it reduces to the Fock interaction energy $J_{\text{ex}} \approx 2U_{\text{Fo}}$.

It is now informative to verify what happens when a small, homogeneous electric field E is applied in the direction connecting to the two dots. This term has two effects: it detunes the two dots leading to a finite dipole moment Δ between the dots and it modifies the tunnel energy $t \to t + \delta t$ due to the change in the potential landscape.

Both effects can be straightforwardly accounted for by conventional perturbation theory. The lowest nontrivial correction in δt and Δ to the exchange energy is given by

$$\delta J_{\text{ex}} = \chi_t \delta t + \chi_\Delta \Delta^2. \tag{B41}$$

The susceptibilities to tunneling and detuning can be found explicitly and they are given by

$$\chi_t = -\frac{2t}{\sqrt{2t^2 + (U_{\text{Hu,Ad}} - U_{\text{Ha,Fo}})^2}}, \tag{B42a}$$

$$\chi_\Delta = \frac{2}{\epsilon_1 - \epsilon_0}\left(1 - \frac{U_{\text{Hu,Ad}} - U_{\text{Ha,Fo}}}{\sqrt{2t^2 + (U_{\text{Hu,Ad}} - U_{\text{Ha,Fo}})^2}}\right). \tag{B42b}$$

These susceptibilities to tunneling and detuning are the ones used in Eqs. (83) and (88).

Note that the lowest order correction is linear in the tunnel energy and quadratic in the detuning. In our model, both these terms lead to a quadratic correction in the electric field, i.e., $\delta J_{\text{ex}} \propto E^2$, because $\Delta \propto E$ and $\delta t \propto E^2$, see Eqs. (B28) and (B29).

APPENDIX C: SOLUTION OF THE HARTREE INTEGRAL

Here, we derive the results presented in Sec. III B. The coupling between two charge densities is captured by the Hartree integral in Eq. (92). We neglect exchange interactions because of the negligible tunnel coupling between the EMP excess charge density and the double dot. We consider a resonator of perimeter L_y, with L_y being much longer than the other lengths in the problem. To define the charge density operator of the double dot system ρ_{D}, we first introduce the charge density operator in the singlet-triplet basis

$$\rho_{\text{ST}} = \rho_S \oplus \rho_T, \tag{C1}$$

with

$$\rho_S = \begin{pmatrix} 2\rho_{11} & 0 & \sqrt{2}\rho_{12} \\ 0 & 2\rho_{22} & \sqrt{2}\rho_{12}^* \\ \sqrt{2}\rho_{12}^* & \sqrt{2}\rho_{12} & \rho_{11} + \rho_{22} \end{pmatrix}, \tag{C2a}$$

$$\rho_T = (\rho_{11} + \rho_{22})\mathcal{I}_3. \tag{C2b}$$

Here, $\mathcal{I}_3$ is the 3×3 identity matrix and ρ_{ij} is the matrix element of the charge density operator in the orthonormal basis

$$\rho = -eP\begin{pmatrix} |\Psi_{00}^-|^2 & (\Psi_{00}^-)^*\Psi_{00}^+ \\ (\Psi_{00}^+)^*\Psi_{00}^- & |\Psi_{00}^+|^2 \end{pmatrix}P. \tag{C3}$$

$\Psi_{00}^{\pm}$ and P are defined in Eqs. (B14) and (B25), respectively.

The charge density ρ_{D} of the eigenstates of the Hamiltonian (B33) is related to ρ_{ST} by a rotation $M_S^\dagger$ acting on the singlet subspace, i.e., $\rho_{\mathrm{D}} = M_S^\dagger \rho_{\mathrm{S}} M_S \oplus \rho_{\mathrm{T}}$. Since we are mainly interested in the situation where the homogeneous electric field E_0 in the x direction is small, we compute the M_S to the first order in perturbation theory and we get

$$M_S = M_S^0\left(1 - 2\sqrt{2}\Delta_1 e E_0\begin{pmatrix} 0 & \frac{A(\epsilon_2)}{\epsilon_1-\epsilon_2} & \frac{A(\epsilon_0)}{\epsilon_1-\epsilon_0} \\ \frac{A(\epsilon_2)}{\epsilon_2-\epsilon_1} & 0 & 0 \\ \frac{A(\epsilon_0)}{\epsilon_0-\epsilon_1} & 0 & 0 \end{pmatrix}\right)C. \tag{C4}$$

Here, M_S^0 is the matrix of normalized column eigenvectors obtained when $E_0 = 0$ and it is given by Eq. (B36). To linear order in E_0, the eigenenergies ϵ_i in Eq. (B38) are unchanged because the first correction is $\propto E_0^2$ [see Eqs. (B28), (B29) and (B41)]. However, the eigenstates of the singlet Hamiltonian are modified by the finite detuning $\Delta_1 e E_0$, leading to the corrections to M_S^0 shown in Eq. (C4). The diagonal matrix $C = \mathrm{diag}(C_1, C_2, C_0)$ is required to renormalize the eigenstates.

We consider now the setup in Fig. 9 and we assume that the QH material has a filling factor $\nu = 1$. In this case, the interaction Hamiltonian reduces to

$$H_{\mathrm{int}} = (M_S^\dagger \kappa_S(q) M_S \oplus \kappa_T(q)) \otimes \hat{a}_q + \mathrm{H.c.}, \tag{C5}$$

where

$$\kappa_T(q) = (\kappa_{11}(q) + \kappa_{22}(q))\mathcal{I}_3, \tag{C6a}$$

$$\kappa_S(q) = \begin{pmatrix} 2\kappa_{11}(q) & 0 & \sqrt{2}\kappa_{12}(q) \\ 0 & 2\kappa_{22}(q) & \sqrt{2}\kappa_{12}^*(-q) \\ \sqrt{2}\kappa_{12}^*(-q) & \sqrt{2}\kappa_{12}(q) & \kappa_{11}(q) + \kappa_{22}(q) \end{pmatrix}. \tag{C6b}$$

We define the 2×2 matrix $\kappa(q) = \kappa^\dagger(-q)$

$$\frac{\kappa(q)}{2\pi} = \frac{\hbar v_p}{L_y}\sqrt{n_q}e^{-(\frac{q l_T}{2})^2} \times P\begin{pmatrix} g(\tau + b_0 + a, q) & s e^{qa\sqrt{\beta}} g(\tau + b_0, q) \\ s e^{qa\sqrt{\beta}} g(\tau + b_0, q) & g(\tau + b_0 - a, q) \end{pmatrix}P, \tag{C7}$$

where b_0 is the shift of the double dot eigenfunctions due to the externally applied electric field E_0 and is defined in Eq. (91). The dimensionless function g depends on the electrostatic configuration of the system; for example in free space $g = g_0$, and

$$g_0(X, q) = \frac{2}{\sqrt{\pi}}\int_{\mathbb{R}} \frac{dx}{\lambda} e^{-\frac{(x-X)^2}{\lambda^2}} K_0(|qx|), \tag{C8}$$

with $\lambda = \sqrt{l'^2 + l_T^2}$.

The presence of a top or side gate at distance d from the EMP center of mass leads to an additive correction to g_0 respectively given by

$$g_t(X, q) = -\frac{2}{\sqrt{\pi}}\int_{\mathbb{R}} \frac{dx}{\lambda} e^{-\frac{(x-X)^2}{\lambda^2}} K_0(|q|\sqrt{x^2 + 4d^2}), \tag{C9a}$$

$$g_s(X, q) \approx -g(X - 2d, q). \tag{C9b}$$

The estimation of g_s is accurate in the limit $d - (\tau + b + a) \gg l_T$ and $d \gg l'$, such that one can safely extend the domain of integration in x and x' from $[-d, \infty)$ to $\mathbb{R}$.

Note that $g_i(X, q)$ introduced here has a similar functional form of the function $g_i(x, q)$ defined in Sec. II B 2 as the projection onto the $z = 0$ plane of the EMP potential. The two definitions coincide if we substitute $l' \to \lambda$ in Eqs. (61) and (66). In particular, we use a small q expansion as in Eq. (62) to approximate g_0, while we use a far-field approximation, analogous to Eq. (63) to estimate $g_{t,s}$. We then obtain

$$g_t(X, q) \approx -2K_0(|q|\sqrt{X^2 + 4d^2}), \tag{C10a}$$

$$g_s(X, q) \approx -2K_0(|q||X - 2d|). \tag{C10b}$$

Also, at small wave vectors ($qa\sqrt{\beta} \ll 1$), the matrix κ is Hermitian and it can be factorized, leading to the conventional electrostatic interaction term $\propto \hat{a}_q^\dagger + \hat{a}_q$.

At this point, we proceed to compute the effective qubit-resonator Hamiltonian. To do so, we make the usual choice of computational basis states, i.e., we take $|\tilde{S}, 0\rangle$ and $|T, 0\rangle$. As long as the qubit energy splitting J_{ex} is close to the resonance frequency of the resonator ω_R, the effective coupling Hamiltonian is efficiently computed by a Schrieffer-Wolff transformation [79]. The lowest order Schrieffer-Wolff Hamiltonian in the long-wavelength and small detuning approximation is

$$H_{\mathrm{eff}}^{(0)} = \frac{J_{\mathrm{ex}}}{2}\sigma_z + \hbar\omega_R \hat{a}^\dagger\hat{a} + \frac{\hbar\gamma}{2}\sigma_z(\hat{a}^\dagger + \hat{a}), \tag{C11}$$

with ω_R being the frequency of the resonator and with the coupling strength being

$$\frac{\gamma}{2\pi} = \frac{v_p\sqrt{n}}{L_y}\left(\frac{\chi_\Delta \Delta_1 e E_0}{\sqrt{1-s^2}}(g(\tau + b_0 - a) - g(\tau + b_0 + a)) + \frac{\sqrt{2}\chi_t s}{1-s^2}\left(g(\tau + b_0) - \frac{g(\tau + b_0 + a) + g(\tau + b_0 - a)}{2}\right)\right). \tag{C12}$$

For simplicity of notation, we dropped the argument q from the function g, the wave number n_q and from the ladder operators $\hat{a}_q$; b_0 is defined in Eq. (91).

Let us consider what happens when $E_0 = 0$ (and so $b_0 = 0$). In this case, we can easily find that γ_1 is given by Eq. (93). As explained in the text, this result is in quantitative agreement with the perturbative solution Eq. (86). This agreement is understood by considering that the term in parentheses in (93) is the discrete gradient of the electric field. This statement is valid if the length l' in the definition of g as the projection in the $z = 0$ plane of Eq. (61) is substituted by λ.

We now attempt to quantify γ_2 by linearizing Eq. (C12) in E_0. With this procedure, we obtain

$$\frac{\gamma_2}{2\pi} \approx -\frac{v_p\sqrt{n}}{2L_y}\frac{2\chi_\Delta\Delta_1 eE_0 a}{\sqrt{1-s^2}}\left(\frac{g(\tau+a)-g(\tau-a)}{a}\right); \tag{C13}$$

we neglected a small additional term of the form

$$\frac{4eE_0\chi_t t_2 v_p\sqrt{n}}{3L_y}\left(\frac{g'(\tau-a)+g'(\tau+a)}{2}-g'(\tau)\right), \tag{C14}$$

where $g'(x)=\partial_x g(x,q)$.

Comparing to the approximate solution in Eq. (94), we find a strong quantitative disagreement even in the far-field limit. The reason formeglio s this disagreement can be traced back to the different approximation scheme used, and, specifically, to the different values of the qubit susceptibility to an homogeneous electric field E calculated in the two approaches.

In the perturbative approach of Sec. III A, in fact, the susceptiblity is found by first projecting the double dot Hamiltonian H_D (B1) onto the subspace of the Hilbert space that is spanned by the E *field-dependent* ground-state wave functions. After this projection, the perturbation theory is formulated in the conventional way by computing the E dependence of the matrix elements of the effective Hamiltonian [see Eqs. (B28) and (B29)] and by finding how much the eigenvectors are rotated by these terms.

In contrast, the Hartree integral approach of Sec. III B follows a different procedure: the perturbation theory is formulated starting from the projection of the Hamiltonian H_D onto the subspace spanned by ground-state wave functions that *do not* depend on E. In other words, to the linear order in E, the single-particle matrix elements H_O^{ij} in Eq. (B26) computed from the Hartree integral do not include the terms

$$E\sum_{\alpha\beta}P_{i\alpha}\left(\frac{\partial}{\partial E}\langle\Psi^{\alpha}_{00}(E)|H_O(E=0)|\Psi^{\beta}_{00}(E)\rangle\right)P_{\beta j}. \tag{C15}$$

These additional terms do not affect the dependence of γ on τ, but they change the susceptibility to E. In fact, neglecting them, we obtain

$$\delta J^{\rm Ha}_{\rm ex} = -2\frac{\chi_\Delta\Delta_1 eE_0 a}{\sqrt{1-s^2}}eE \tag{C16}$$

instead of Eq. (88). Equation (C16) is consistent with the value of γ_2 shown in Eq. (C13) in the same sense discussed for γ_1, i.e., if we interpret E in (C16) as the discrete derivative of the EMP voltage in Eq. (C13).

This interpretation suggests a possible ad-hoc modification of Eq. (C13) to include a posteriori the terms neglected in the Hartree approach. Namely, we use the susceptibility from Eq. (88) instead of the one in Eq. (C16). By performing the substitution

$$\frac{\chi_\Delta\Delta_1 a}{\sqrt{1-s^2}} \to -\left(\chi_t t_2+\chi_\Delta\Delta_1^2\right), \tag{C17}$$

in Eq. (C13) and setting $n=1$, we obtain Eq. (94).

Note that if we were to consider the rotated configuration, with the two dots aligned to the resonator edge, in the long-wavelength limit, Eq. (C12) is valid if we make the substitutions $a\to ia\sqrt{\beta}$ and $b_0\to 0$. In this case, as expected, an homogeneous electric field E_0 parallel to the resonator edge has no effect, since the term linear in E_0 is $\propto \ \mathrm{Im}(g(\tau+ia\sqrt{\beta}))=0$.

Finally, the effective Hamiltonian (C11) captures the behavior of the system as long as the coupling between the computational and the noncomputational subspaces of the double dot can be neglected, i.e., when

$$\zeta \equiv \max\left|\frac{(M_S^{\dagger}\kappa_S M_S)_{3,i}}{\epsilon_0-\epsilon_i\pm\hbar\omega_R}\right| \ll 1; \tag{C18}$$

the value 3 in the index of the matrix product comes from the chosen ordering of the eigenenergies.

---

[1] K. v. Klitzing, G. Dorda, and M. Pepper, New Method for High-Accuracy Determination of the Fine-Structure Constant based on Quantized Hall Resistance, Phys. Rev. Lett. **45**, 494 (1980).

[2] M. E. Cage, K. Von Klitzing, A. M. Chang, F. Duncan, M. Haldane, R. B. Laughlin, A. M. M. Pruisken, D. J. Thouless, R. E. Prange, and S. M. Girvin, *The Quantum Hall Effect* (Springer Science & Business Media, 2012).

[3] K. von Klitzing, The quantized hall effect, Rev. Mod. Phys. **58**, 519 (1986).

[4] D. J. Thouless, M. Kohmoto, M. P. Nightingale, and M. den Nijs, Quantized Hall Conductance in a Two-Dimensional Periodic Potential, Phys. Rev. Lett. **49**, 405 (1982).

[5] R. B. Laughlin, Quantized hall conductivity in two dimensions, Phys. Rev. B **23**, 5632 (1981).

[6] W. Poirier and F. Schopfer, Resistance metrology based on the quantum hall effect, Eur. Phys. J. Special Topics **172**, 207 (2009).

[7] T. M. Stace, C. H. W. Barnes, and G. J. Milburn, Mesoscopic One-Way Channels for Quantum State Transfer via the Quantum Hall Effect, Phys. Rev. Lett. **93**, 126804 (2004).

[8] G. Viola and D. P. DiVincenzo, Hall Effect Gyrators and Circulators, Phys. Rev. X **4**, 021019 (2014).

[9] R. F. Wick, Low-loss hall-effect devices US Patent 3,214,682 (1965).

[10] B. Placke, S. Bosco, and D. P. DiVincenzo, A model study of present-day hall-effect circulators, EPJ Quantum Technology **4**, 5 (2017).

[11] S. Bosco, F. Haupt, and D. P. DiVincenzo, Self-Impedance-Matched Hall-Effect Gyrators and Circulators, Phys. Rev. Appl. **7**, 024030 (2017).

[12] A. C. Mahoney, J. I. Colless, S. J. Pauka, J. M. Hornibrook, J. D. Watson, G. C. Gardner, M. J. Manfra, A. C. Doherty, and D. J. Reilly, On-Chip Microwave Quantum Hall Circulator, Phys. Rev. X **7**, 011007 (2017).

[13] C. Müller, S. Guan, N. Vogt, J. H. Cole, and T. M. Stace, Passive On-Chip Superconducting Circulator using a Ring of Tunnel Junctions, Phys. Rev. Lett. **120**, 213602 (2018).

[14] J. Koch, A. A. Houck, K. L. Hur, and S. M. Girvin, Time-reversal-symmetry breaking in circuit-qed-based photon lattices, Phys. Rev. A **82**, 043811 (2010).

[15] S. Bosco, D. P. DiVincenzo, and D. J. Reilly, Transmission lines and metamaterials based on quantum hall plasmonics, arXiv:1812.02976 [Phys. Rev. Appl. (to be published)].

[16] D. M. Pozar, *Microwave Engineering*, 4th ed. (Wiley, 2011).

[17] A. Stockklauser, P. Scarlino, J. V. Koski, S. Gasparinetti, C. K. Andersen, C. Reichl, W. Wegscheider, T. Ihn, K. Ensslin, and A. Wallraff, Strong Coupling Cavity QED with Gate-Defined Double Quantum Dots Enabled by a High Impedance Resonator, Phys. Rev. X **7**, 011030 (2017).

[18] A. J. Landig, J. V. Koski, P. Scarlino, U. C. Mendes, A. Blais, C. Reichl, W. Wegscheider, A. Wallraff, K. Ensslin, and T. Ihn, Coherent spin-qubit photon coupling using a resonant exchange qubit, Nature (London) **560**, 179 (2018).

[19] S. J. Elman, S. D. Bartlett, and A. C. Doherty, Long-range entanglement for spin qubits via quantum hall edge modes, Phys. Rev. B **96**, 115407 (2017).

[20] S. P. Harvey, C. G. L. Bøttcher, L. A. Orona, S. D. Bartlett, A. C. Doherty, and A. Yacoby, Coupling two spin qubits with a high-impedance resonator, Phys. Rev. B **97**, 235409 (2018).

[21] M. Benito, M. J. A. Schuetz, J. I. Cirac, G. Platero, and G. Giedke, Dissipative long-range entanglement generation between electronic spins, Phys. Rev. B **94**, 115404 (2016).

[22] V. E. Manucharyan, J. Koch, L. I. Glazman, and M. H. Devoret, Fluxonium: Single cooper-pair circuit free of charge offsets, Science **326**, 113 (2009).

[23] N. A. Masluk, I. M. Pop, A. Kamal, Z. K. Minev, and M. H. Devoret, Microwave Characterization of Josephson Junction Arrays: Implementing a Low Loss Superinductance, Phys. Rev. Lett. **109**, 137002 (2012).

[24] A. J. Annunziata, D. F. Santavicca, L. Frunzio, G. Catelani, M. J. Rooks, A. Frydman, and D. E. Prober, Tunable superconducting nanoinductors, Nanotechnology **21**, 445202 (2010).

[25] D. F. Santavicca, J. K. Adams, L. E. Grant, A. N. McCaughan, and K. K. Berggren, Microwave dynamics of high aspect ratio superconducting nanowires studied using self-resonance, J. Appl. Phys. **119**, 234302 (2016).

[26] D. Niepce, J. Burnett, and J. Bylander, High Kinetic Inductance Nb N Nanowire Superinductors, Phys. Rev. Appl. **11**, 044014 (2019).

[27] M. J. Hagmann, Isolated carbon nanotubes as high-impedance transmission lines for microwave through terahertz frequencies, IEEE Trans. Nanotechnol. **4**, 289 (2005).

[28] C. Altimiras, O. Parlavecchio, P. Joyez, D. Vion, P. Roche, D. Esteve, and F. Portier, Tunable microwave impedance matching to a high impedance source using a josephson metamaterial, Appl. Phys. Lett. **103**, 212601 (2013).

[29] P. J. Burke, Luttinger liquid theory as a model of the gigahertz electrical properties of carbon nanotubes, IEEE Trans. Nanotechnol. **1**, 129 (2002).

[30] J. D. Chudow, D. F. Santavicca, and D. E. Prober, Terahertz spectroscopy of individual single-walled carbon nanotubes as a probe of luttinger liquid physics, Nano Lett. **16**, 4909 (2016).

[31] M. Benito, X. Mi, J. M. Taylor, J. R. Petta, and G. Burkard, Input-output theory for spin-photon coupling in si double quantum dots, Phys. Rev. B **96**, 235434 (2017).

[32] X. Mi, M. Benito, S. Putz, D. M. Zajac, J. M. Taylor, G. Burkard, and J. R. Petta, A coherent spin-photon interface in silicon, Nature (London) **555**, 599 (2018).

[33] X. Mi, J. V. Cady, D. M. Zajac, P. W. Deelman, and J. R. Petta, Strong coupling of a single electron in silicon to a microwave photon, Science **355**, 156 (2016).

[34] R. F. Wick, Solution of the field problem of the germanium gyrator, J. Appl. Phys. **25**, 741 (1954).

[35] R. W. Rendell and S. M. Girvin, Hall voltage dependence on inversion-layer geometry in the quantum hall-effect regime, Phys. Rev. B **23**, 6610 (1981).

[36] V. A. Volkov and S. A. Mikhailov, Edge magnetoplasmons-low-frequency weakly damped excitations in homogeneous two-dimensional electron systems, Zh. Eksp. Teor. Fiz. **94**, 217 (1988).

[37] M. D. Johnson and G. Vignale, Dynamics of dissipative quantum hall edges, Phys. Rev. B **67**, 205332 (2003).

[38] I. L. Aleiner and L. I. Glazman, Novel Edge Excitations of Two-Dimensional Electron Liquid in a Magnetic Field, Phys. Rev. Lett. **72**, 2935 (1994).

[39] I. L. Aleiner, D. Yue, and L. I. Glazman, Acoustic excitations of a confined two-dimensional electron liquid in a magnetic field, Phys. Rev. B **51**, 13467 (1995).

[40] J. C. W. Song and M. S. Rudner, Chiral plasmons without magnetic field, Proc. Natl. Acad. Sci. USA **113**, 4658 (2016).

[41] A. C. Mahoney, J. I. Colless, L. Peeters, S. J. Pauka, E. J. Fox, X. Kou, L. Pan, K. L. Wang, D. Goldhaber-Gordon, and D. J. Reilly, Zero-field edge plasmons in a magnetic topological insulator, Nat. Commun. **8**, 1836 (2017).

[42] N. Kumada, P. Roulleau, B. Roche, M. Hashisaka, H. Hibino, I. Petković, and D. C. Glattli, Resonant Edge Magnetoplasmons and Their Decay in Graphene, Phys. Rev. Lett. **113**, 266601 (2014).

[43] M. Hashisaka, H. Kamata, N. Kumada, K. Washio, R. Murata, K. Muraki, and T. Fujisawa, Distributed-element circuit model of edge magnetoplasmon transport, Phys. Rev. B **88**, 235409 (2013).

[44] U. Zülicke and A. H. MacDonald, Plasmon modes and correlation functions in quantum wires and hall bars, Phys. Rev. B **54**, 16813 (1996).

[45] S. Bosco and D. P. DiVincenzo, Nonreciprocal quantum hall devices with driven edge magnetoplasmons in two-dimensional materials, Phys. Rev. B **95**, 195317 (2017).

[46] S. A. Mikhailov, Edge and inter-edge magnetoplasmons in two-dimensional electron systems, in *Edge Excitations of Low-Dimensional Charged Systems* (Max-Planck Institute for the Physic of complex Systems, Dresden, Germany, 2001), pp. 1.

[47] J. H. Han and D. J. Thouless, Dynamics of compressible edge and bosonization, Phys. Rev. B **55**, 1926(R) (1997).

[48] H. L. Störmer, J. P. Eisenstein, A. C. Gossard, W. Wiegmann, and K. Baldwin, Quantization of the Hall Effect in an Anisotropic Three-Dimensional Electronic System, Phys. Rev. Lett. **56**, 85 (1986).

[49] A. Briggs, Y. Guldner, J. P. Vieren, M. Voos, J. P. Hirtz, and M. Razeghi, Low-temperature investigations of the quantum hall effect in $\mathrm{In}_x\mathrm{ga}_{1-x}\mathrm{As}-\mathrm{InP}$ heterojunctions, Phys. Rev. B **27**, 6549(R) (1983).

[50] E. J. Fox, I. T. Rosen, Y. Yang, G. R. Jones, R. E. Elmquist, X. Kou, L. Pan, K. L. Wang, and D. Goldhaber-Gordon, Part-per-million quantization and current-induced breakdown of the quantum anomalous hall effect, Phys. Rev. B **98**, 075145 (2018).

[51] A. J. Bestwick, E. J. Fox, X. Kou, L. Pan, K. L. Wang, and D. Goldhaber-Gordon, Precise Quantization of the Anomalous Hall Effect Near Zero Magnetic Field, Phys. Rev. Lett. **114**, 187201 (2015).

[52] J. Levy, Quantum-information processing with ferroelectrically coupled quantum dots, Phys. Rev. A **64**, 052306 (2001).

[53] L. Banszerus, M. Schmitz, S. Engels, J. Dauber, M. Oellers, F. Haupt, K. Watanabe, T. Taniguchi, B. Beschoten, and C. Stampfer, Ultrahigh-mobility graphene devices from chemical vapor deposition on reusable copper, Sci. Adv. **1**, e1500222 (2015).

[54] F. D. Parmentier, T. Cazimajou, Y. Sekine, H. Hibino, H. Irie, D. C. Glattli, N. Kumada, and P. Roulleau, Quantum hall effect in epitaxial graphene with permanent magnets, Sci. Rep. **6**, 38393 (2016).

[55] J. D. Sanchez-Yamagishi, J. Y. Luo, A. F. Young, B. M. Hunt, K. Watanabe, T. Taniguchi, R. C. Ashoori, and P. Jarillo-Herrero, Helical edge states and fractional quantum hall effect in a graphene electron–hole bilayer, Nat. Nanotechnol. **12**, 118 (2017).

[56] S. Richer and D. P. DiVincenzo, Circuit design implementing longitudinal coupling: A scalable scheme for superconducting qubits, Phys. Rev. B **93**, 134501 (2016).

[57] S. Richer, N. Maleeva, S. T. Skacel, I. M. Pop, and D. P. DiVincenzo, Inductively shunted transmon qubit with tunable transverse and longitudinal coupling, Phys. Rev. B **96**, 174520 (2017).

[58] N. Didier, J. Bourassa, and A. Blais, Fast Quantum Nondemolition Readout by Parametric Modulation of Longitudinal Qubit-Oscillator Interaction, Phys. Rev. Lett. **115**, 203601 (2015).

[59] M. Russ and G. Burkard, Three-electron spin qubits, J. Phys.: Condens. Matter **29**, 393001 (2017).

[60] G. Giuliani and G. Vignale, *Quantum Theory of the Electron Liquid*, 1st ed. (Cambridge University Press, New York, 2008).

[61] I. Petković, F. I. B. Williams, and D. C. Glattli, Edge magnetoplasmons in graphene, J. Phys. D **47**, 094010 (2014).

[62] I. Petković, F. I. B. Williams, K. Bennaceur, F. Portier, P. Roche, and D. C. Glattli, Carrier Drift Velocity and Edge Magnetoplasmons in Graphene, Phys. Rev. Lett. **110**, 016801 (2013).

[63] J. Larsson, Electromagnetics from a quasistatic perspective, Am. J. Phys. **75**, 230 (2007).

[64] H. A. Haus and J. R. Melcher, *Electromagnetic Fields and Energy* (Prentice-Hall: Englewood Cliffs, NJ, 1989).

[65] A. H. MacDonald, T. M. Rice, and W. F. Brinkman, Hall voltage and current distributions in an ideal two-dimensional system, Phys. Rev. B **28**, 3648 (1983).

[66] M. Abramowitz and I. A. Stegun, *Handbook of Mathematical Functions: with Formulas, Graphs, and Mathematical Tables* (Courier Corporation, 1964), Vol. 55.

[67] G. Rousseaux, Lorenz or coulomb in galilean electromagnetism? Europhys. Lett. **71**, 15 (2005).

[68] R. C. Ashoori, H. L. Stormer, L. N. Pfeiffer, K. W. Baldwin, and K. West, Edge magnetoplasmons in the time domain, Phys. Rev. B **45**, 3894 (1992).

[69] D. B. Chklovskii, B. I. Shklovskii, and L. I. Glazman, Electrostatics of edge channels, Phys. Rev. B **46**, 4026 (1992).

[70] G. Yang, C.-H. Hsu, P. Stano, J. Klinovaja, and D. Loss, Long-distance entanglement of spin qubits via quantum hall edge states, Phys. Rev. B **93**, 075301 (2016).

[71] G. Burkard, D. Loss, and D. P. DiVincenzo, Coupled quantum dots as quantum gates, Phys. Rev. B **59**, 2070 (1999).

[72] S. E. Nigg, R. López, and M. Büttiker, Mesoscopic Charge Relaxation, Phys. Rev. Lett. **97**, 206804 (2006).

[73] M. Mariantoni, F. Deppe, A. Marx, R. Gross, F. K. Wilhelm, and E. Solano, Two-resonator circuit quantum electrodynamics: A superconducting quantum switch, Phys. Rev. B **78**, 104508 (2008).

[74] H. Bluhm, S. Foletti, D. Mahalu, V. Umansky, and A. Yacoby, Enhancing the Coherence of a Spin Qubit by Operating It As a Feedback Loop That Controls its Nuclear Spin Bath, Phys. Rev. Lett. **105**, 216803 (2010).

[75] H. Bluhm, S. Foletti, I. Neder, M. Rudner, D. Mahalu, V. Umansky, and A. Yacoby, Dephasing time of gaas electron-spin qubits coupled to a nuclear bath exceeding 200 μs, Nat. Phys. **7**, 109 (2011).

[76] C. de C. Chamon and X. G. Wen, Sharp and smooth boundaries of quantum hall liquids, Phys. Rev. B **49**, 8227 (1994).

[77] X. G. Wen, Chiral luttinger liquid and the edge excitations in the fractional quantum hall states, Phys. Rev. B **41**, 12838 (1990).

[78] E. Barnes, J. P. Kestner, N. T. T. Nguyen, and S. Das Sarma, Screening of charged impurities with multielectron singlet-triplet spin qubits in quantum dots, Phys. Rev. B **84**, 235309 (2011).

[79] S. Bravyi, D. P. DiVincenzo, and D. Loss, Schrieffer-wolff transformation for quantum many-body systems, Ann. Phys. **326**, 2793 (2011).